الجمهورية الجزائرية الديمقراطية الشعبية People's Democratic Republic of Algeria

وزارة التعليم السعبائي و البحث العسلمسي Ministry of Higher Education and Scientific Research

> جامعة سعد دحلب البليدة SAAD DAHLAB University of BLIDA

> > كلية التكنولوجيا Faculty of Technology

قسم الإلكترونيك Department of Electronics



Master's thesis

Field Electronics
Specialty Embedded Systems Electronics

Presented by

Naluwuge Rashidah Kakooza

&

Seiafa Rania

Modelisation and Conception of a Michelson Interferometer based on Digital Micromirrors

Proposed by: Mme Nadia Bougherira & Mme Hamida Bougherira
University Year 2024-2025

We would like to express our deepest gratitude to Allah for His endless blessings and for guiding us every step of the way throughout this journey.

We would like to extend our sincere thanks to all the professors who have accompanied us during our academic path. Your dedication, your knowledge, and your commitment have been instrumental in our growth and in shaping us into the engineers we are today.

In a very special way, we would like to express our heartfelt appreciation to our supervisors, Madam Nadia Bougherira and Madame Hamida Bougherira. You walked with us every step of the way, contributing tirelessly and generously to every stage of this research. Your constant guidance, encouragement, and belief in us pushed us to give our very best. We are deeply grateful for your support, your patience, and the trust you placed in us throughout this project.

To my beloved mother, thank you for believing in every dream I've ever had, even the ones that seemed far from reach. You never placed limits on my ambitions. Instead, you trusted me to pursue my studies in countries far from home and believed that I would carry with me every lesson and value you taught me, to make wise decisions for my life. You supported me from afar, prayed for me endlessly, and carried the weight of this dream, financially and emotionally. I am everything I am because of your strength, faith, and love.

To my amazing siblings, your sacrifices, your encouragement, and your constant presence, even from miles away in Uganda, have been my greatest support system. You reminded me every day that my dreams are valid and that I'm never alone in this journey. This achievement is yours as much as it is mine.

To my girls, Nabagala Immaculate, Nalumansi Alexis Edith, and Kayaga Latifa, I don't know what life in Algeria would have been without you. You were my family away from home, my comfort, my encouragement, and my joy. Thank you for your unconditional support, for affirming me when I doubted myself, and for helping me push through the hardest moments. You made everything bearable.

To Elizesta Nhacupatoma and Zinhle Ndlovu, you were the big sisters I never knew I needed. From the day I arrived in Blida, you took me under your wing, taught me how to survive in this new world, and created a safe space where I could grow and thrive. I will forever be grateful for your kindness, strength, and guidance.

This work is dedicated to all of you, my anchors, my light, and my reason to keep going.

To my two supervisors, your guidance, patience, and encouragement have been invaluable to me. As strong women in science, you have not only mentored me academically but have also inspired me on a personal level. Thank you for believing in my potential and for helping me grow as both a student and a future engineer.

To my family, words are not enough to thank you for your unwavering love and support. Your sacrifices, your faith in me, and your constant encouragement have been the foundation of everything I have achieved. You are my strength and my motivation, and I owe you everything.

To my dear friend Chaima, thank you for being by my side through every step of this journey. Your kindness, your understanding, and your friendship have meant the world to me. I am grateful for the laughter, the long talks, and all the moments that made this experience lighter and brighter.

Finally, to my grandfather Said, even though you may no longer be physically with us, your presence, your wisdom and love have always guided me. You are forever in my heart, and this accomplishment is dedicated to you as well.

This work is more than the result of academic effort; it is a reflection of the love, support, and kindness that I have been lucky enough to receive.

:ملخص

يستكشف هذا البحث تصميم ومحاكاة مقياس تداخل ميكلسون المعدل الذي يهدف إلى تحسين التصوير المقطعي التوافقي من خلال دمج المرايا الرقمية الدقيقة. من خلال استبدال المرآة المرجعية الثابتة بمرايا دقيقة يتم التحكم فيها (OCT) البصري المسح الضوئي مما يزيد -A المسح الضوئي-A بشكل مستقل، يتيح النظام إمكانية الحصول على المسح الضوئي المتوازي، قمنا بمحاكاة تكوينات أحادية الحزمة ومتعددة COMSOL Multiphysics من سرعة التصوير بشكل كبير. باستخدام الحزم لتحليل تأثير تباين المسار البصري على أنماط التداخل ودقة العمق

، مقياس التداخل ميشيلسون، المرايا الدقيقة الرقمية(OCT) التصوير المقطعي التوافقي البصري : كلمات المفاتيح

Résumé:

Cette recherche porte sur la conception et la simulation d'une version modifiée de l'interféromètre de Michelson, dans le but d'améliorer la Tomographie par Cohérence Optique (OCT) grâce à l'intégration de micromiroirs numériques. En remplaçant le miroir de référence fixe par des micromiroirs contrôlés individuellement, le système permet l'acquisition parallèle de scans A, augmentant considérablement la vitesse d'imagerie. À l'aide de COMSOL Multiphysics, nous avons simulé des configurations à un et plusieurs faisceaux afin d'analyser l'effet de la variation du chemin optique sur les franges d'interférence et la résolution en profondeur.

Mots clés : Tomographie par cohérence optique (OCT), Interféromètre de Michelson, Micromiroirs numériques

Abstract:

This research explores the design and simulation of a modified Michelson interferometer aimed at improving Optical Coherence Tomography (OCT) through the integration of digital micromirrors. By replacing the static reference mirror with independently controlled micromirrors, the system enables parallel A-scan acquisition, significantly increasing imaging speed. Using COMSOL Multiphysics, we simulated single-beam and multi-beam configurations to analyze the impact of optical path variation on interference patterns and depth resolution.

Keywords: Optical Coherence Tomography, Michelson interferometer, Digital micromirror

Abbreviation List

CTE: Coefficients of Thermal Expansion.

DLP: Digital Light Processing.

FD-OCT: Fourier-Domain Optical Coherence Tomography.

FWHM: Full Width at Half Maximum.

LCI: Low-Coherence Interferometry.

LED: Light Emitting Diode.

MEMS: Micro Electro-Mechanical Systems.

OCT: Optical Coherence Tomography.

OPD: Optical Path Difference.

RPE: Retinal Pigment Epithelium.

SD-OCT: Spectral-Domain Optical Coherence Tomography.

SS-OCT: Swept-Source Optical Coherence Tomography

TD-OCT: Time-Domain Optical Coherence Tomography.

Table of Contents

General Introduction	
Chapter 1	3
Optical Principles and the Michelson Interferometer	4
1.1. Introduction	4
1.2 Anatomy of the eye	5
1.2.1 Retina	
1.3 General terms related to light	
1.3.1 Young's double-slit experiment	
1.3.2 Calculating the intensity of fringes in Young's double-slit experiment	
1.4 Interference of light	
1.4.1 Constructive interference	13
1.4.2 Destructive interference	14
1.5 Coherence	16
1.5.1 Temporal coherence	16
1.5.2 Spatial coherence	17
1.6 Interferometry	18
1.6.1 Michelson interferometer	19
1.6.2 Principle of Operation of the Michelson interferometer	19
1.6.3 Path Difference & Fringe Formation	20
1.6.4 Coherence length	21
1.6.5 Calculation of light intensity detected	21
1.7 Applications of Michelson interferometer	21
1.8 Conclusion.	22
Chapter 2	24
OCT and Digital Micromirrors	
2.1. Introduction	25
2.2. Optical Coherence Tomography (OCT)	
2.2.1 Principle of low-coherence interferometry	
2.2.2 Intensity of light on the photodiode in OCT	27
2.2.3 Depth Movement	28
2.2.4 Processing an OCT signal	29
2.2.5 Stratified medium	29

2.2.6 Scanning modes in OCT
2.2.7 Types of OCT
2.3.2 Types of micromirrors
2.3.3 Applications of digital micromirrors
Chapter 3:
Design, Implementation and Simulation of a Michelson Interferometer based on Digital Micromirrors 44
3.1 Introduction
3.2Conceptual Development of Micromirror-Based Michelson Interferometer Configurations 47
3.2.1 Single-Beam Michelson Interferometer Configuration with One Micromirror
3.2.2 Dual-Beam Michelson Interferometer Configuration with Two Micromirrors
3.2.3 Dual-Beam Michelson Interferometer Configuration with Two Micromirrors50
3.2.4 Triple-Beam Michelson Interferometer Configuration with Three Micromirrors 50
3.2.5 Four-Beam Configuration with Three Micromirrors and a Three-Layer Sample
3.3 Simulation and Analysis Using COMSOL Multiphysics
3.3.1 Interferometer Setup in COMSOL 53
3.3.2 Configuration of a single-beam Michelson interferometer with 1 micromirror54
3.3.3 Configuration of multiple-beam Michelson interferometer with a micromirror array 58
3.4 Discussion of results
3.5 General conclusion

List of figures

Figure 1.1: Photo showing anatomy of the eye5
Figure 1.2: Photo of the retina showing cones and rods6
Figure 1.3: Layers of the retina7
Figure 1.4: Refraction of light9
Figure 1.5: Diffraction of light
Figure 1.6: Young's double-slit experiment
Figure 1.7: Fringes on the screen in Young's double slit experiment
Figure 1.8: Constructive Interference
Figure 1.9: Destructive Interference
Figure 1.10: Spatial and temporal coherence
Figure 1.11: Michelson interferometer
Figure 2.1: Low-Coherence interferometer
Figure 2.2: OCT signal before processing
Figure 2.3: OCT signal after processing
Figure 2.4: Stratified medium composed of 3 layers with different refractive indices29
Figure 2.5: Interferometric signal detected on the photodiode when the sample arm has a biological tissue with different refractive indices
Figure 2.6: Signal after demodulation showing 3 peaks corresponding to the 3 interfaces30
Figure 2.7: Low-coherence beam scanning through multilayer sample31
Figure 2.8: A-scan of the eye
Figure 2.9: B-scan of the eye34

Figure 2.10: C-scan of the eye
Figure 2.11: Time-Domain OCT
Figure 2.12: Spectral-Domain and Swept-Source OCT
Figure 2.13: Digital micromirror
Figure 3.1: Michelson interferometer configuration where the beam splitter is replaced by a set of micromirrors
Figure 3.2: Michelson interferometer configuration where the light source is parallelized46
Figure 3.3: Michelson interferometer configuration with micromirrors in the reference Arm
Figure 3.4: Single-beam Michelson interferometer configuration
Figure 3.5: Dual-beam Michelson Interferometer Configuration
Figure 3.6: Dual-beam Michelson Interferometer Configuration
Figure 3.7: 3-Beam Michelson Interferometer Configuration
Figure 3.8: 4-beam Michelson Interferometer Configuration
Figure 3.9: Parameters for the configuration of the Michelson interferometer in COMSOL53
Figure 3.10: Single-beam Michelson interferometer
Figure 3.11: Interference pattern at delta_d=600 x lam
Figure 3.12: Extracted depth profile showing intensity as a function of optical path difference (delta_d)
Figure 3.13: Dual-beam Michelson interferometer
Figure 3.14: Interference pattern of Ray 1 at delta_d=600 x lam61
Figure 3.15: Interference pattern of Ray 2 at delta_d=600 x lam61
Figure 3.16: Extracted depth profile showing intensity as a function of optical path difference (delta_d) for Ray 1
Figure 3.17: Extracted depth profile showing intensity as a function of optical path difference (delta_d) for Ray 2

Figure 3.18: Dual-beam Michelson interferometer	63
Figure 3.19: Interference pattern of Ray 1 at delta_d=600 x lam	64
Figure 3.20: Interference pattern of Ray 2 at delta_d=600 x lam	64
Figure 3.21: Extracted depth profile showing intensity as a function of optical path difference (delta_d) for Ray 1	64
Figure 3.22: Extracted depth profile showing intensity as a function of optical path difference (delta_d) for Ray 2	65
Figure 3.23: 3-beam Michelson interferometer	66
Figure 3.24: Interference pattern of Ray 1 at delta_d=600 x lam	67
Figure 3.25: Interference pattern of Ray 2 at delta_d=600 x lam	67
Figure 3.26: Interference pattern of Ray 3 at delta_d=600 x lam	67
Figure 3.27: Extracted depth profile showing intensity as a function of optical path difference (delta_d) for Ray 1	67
Figure 3.28: Extracted depth profile showing intensity as a function of optical path difference (delta_d) for Ray 2	68
Figure 3.29: Extracted depth profile showing intensity as a function of optical path difference (delta_d) for Ray 3	68
Figure 3.30: 4-beam Michelson interferometer configuration	70
Figure 3.31: Interference pattern of Ray 1 at delta_d=600 x lam	70
Figure 3.32: Interference pattern of Ray 2 at delta_d=600 x lam	70
Figure 3.33: Interference pattern of Ray 3 at delta_d=600 x lam	70
Figure 3.34: Interference pattern of Ray 4 at delta_d=600 x lam	70
Figure 3.35: Extracted depth profile showing intensity as a function of optical path difference (delta_d) for Ray 1	71
Figure 3.36: Extracted depth profile showing intensity as a function of optical path difference (delta_d) for Ray 2	71
Figure 3.37: Extracted depth profile showing intensity as a function of optical path difference (delta_d) for Ray 3	72

Figure 3.38: Extracted depth profile showing intensity as a function of optical path
difference (delta_d) for Ray472

List of tables

Table 1.1: Retinal layers and optical properties	8
Table 3.1: Parameters for single-beam Michelson setup	47
Table 3.2: Parameters for dual-beam configuration	48
Table 3.3: Parameters for three-beam configuration	49
Table 3.4: Parameters for four-beam configuration	50
Table 3.5: COMSOL simulation input summary	51

General Introduction

The study of light and its relationships with various forms of matter has facilitated advances in optical imaging systems. Among these advances is Optical Coherence Tomography (OCT), a powerful non-invasive imaging technique that enables the rapid capture of high-resolution cross-sectional images of biological tissues such as the human retina. At the heart of OCT is the Michelson interferometer, a fundamental optical instrument that enables deep imaging by analyzing the interference patterns created by reflected light beams with varying optical path lengths. The operating principle of OCT is based on low-coherence interferometry, typically implemented by a Michelson interferometer. The main challenge addressed in this thesis is the limitation of traditional OCT systems, which rely on mechanical scanning in the reference arm, thus limiting imaging speed and efficiency. In this work, we propose an innovative redesign of the traditional Michelson interferometer by replacing its reference arm with a digital micromirror array. This integration enables parallel OCT scans.

Chapter 1 reviews the fundamental phenomena of light, including diffraction, refraction, and interference. This chapter is based on Young's double-slit experiment, which provided the first clear evidence of light interference and fringe formation through constructive and destructive interference. A thorough discussion of temporal and spatial coherence is also presented, as they are crucial for the formation and stability of interference fringes. This chapter also discusses the anatomy of the retina, highlighting its layered structure with different refractive indices. Understanding these layers is essential because OCT depth imaging relies on the detection of backscattered light from interfaces where refractive indices change, thus enabling the reconstruction of depth-resolved images of retinal tissue. The chapter concludes with a detailed analysis of the Michelson interferometer, including the mathematical modeling of the fringe intensity patterns that form the basis of OCT measurements.

Chapter 2 focuses on OCT itself, describing its operating principles, including various techniques such as time-domain OCT, spectral-domain OCT, and swept-source OCT, as well as the different

scanning types (A-scan, B-scan, and C-scan). This chapter also introduces digital micromirrors, discussing their types, actuation methods, and integration into optical systems. It explores the potential of micromirrors to enable parallel multibeam scanning in OCT, which can significantly improve imaging speed and system performance.

Chapter 3 discusses the modeling and design of the Michelson interferometer integrating a digital micromirror array in the reference arm. The simulations, performed with COMSOL Multiphysics, include a sample representing the retina, composed of multiple layers of distinct refractive indices, to realistically reproduce depth-dependent reflection OCT measurements. The integration of the micromirror array aims to dynamically control the reference arm, thus enabling parallel interferometric measurements. This addition facilitates the parallelization of OCT scans, thus significantly improving imaging speed and system performance. This chapter presents the design, optical configuration, and simulation results, demonstrating how such a system could enhance OCT imaging capabilities by accelerating acquisition and enabling flexible scanning architectures. This project aims to combine classical interferometry with modern micromirror technology, proposing a flexible and digitally reconfigurable Michelson interferometer architecture that can advance OCT systems towards faster, more adaptable and higher resolution imaging.

Chapter 1

Optical Principles and the Michelson interferometer

Optical Principles and the Michelson Interferometer

1.1 <u>Introduction</u>

There has been a lot of research into how light interacts with biological tissues, especially in the area of biomedical optics. The human retina is one of the most complex and delicate organs that interacts with light. The development of sophisticated imaging methods, like Optical Coherence Tomography (OCT), which is based on the concepts of interference and coherence, depends on an understanding of how light interferes within retinal structures.

This chapter establishes the theoretical basis for understanding the optical principles that support interferometric systems such as the Michelson interferometer and their application in advanced imaging modalities. These foundational concepts are essential for appreciating the role of light manipulation, coherence, and interference in technologies like OCT.

This chapter establishes the theoretical basis for understanding the optical principles that form the foundation of interferometric systems such as the Michelson interferometer and their application in advanced imaging modalities. These foundational concepts are essential for appreciating the role of light manipulation.

1.2 Anatomy of the eye

The human eye is an organ responsible for vision. Its structure is designed to capture light and convert it into electrical signals, enabling the brain to perceive images.

Primary structures

- Cornea: The clear, dome-shaped front part of the eye that focuses incoming light.
- Sclera: The white, outer layer of the eye that maintains its shape and provides protection.
- **Conjunctiva**: A thin membrane covering the sclera and inner eyelids, aiding in lubrication and protection.
- **Iris**: The colored part of the eye containing muscles that regulate the size of the pupil to control light entry.
- Pupil: The central opening in the iris that adjusts to allow varying amounts of light to reach the
 retina.
- Lens: A transparent structure behind the iris that changes shape to focus light onto the retina.
- **Retina**: The inner layer at the back of the eye containing photoreceptor cells (rods and cones) that convert light into neural signals.
- Macula: A small central area in the retina responsible for detailed central vision.
- Optic Nerve: The nerve that transmits visual information from the retina to the brain.
- Choroid: A vascular layer between the retina and sclera that supplies blood to the eye

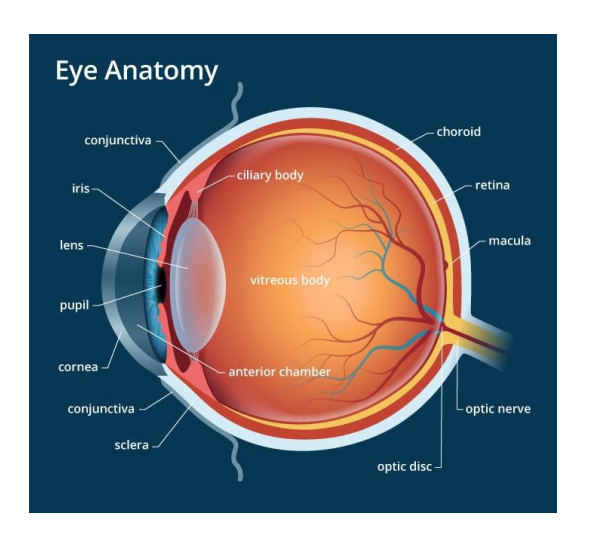


Figure 1.1: Photo showing the anatomy of the eye

1.2.1 Retina

The retina is a layer of photoreceptors cells (rods and cones), glial cells (Müller glial cells, Astrocytes and Microglia cells) and neurons within the eye, that captures incoming photons and transmits them along neuronal pathways as both electrical and chemical signals for the brain to perceive a visual picture.

Rods are photoreceptor cells specialized for vision in low-light conditions and provide black-and-white vision. They are crucial for night vision and peripheral vision. There are approximately 120 million rods in the human retina located mostly in the peripheral regions of the retina and are absent in the fovea.

Cones are more sensitive in daylight and capture wavelengths of colored light. They are located in the center of the retina at the fovea. There are approximately 6 million cones in the retina. There are three subtypes of cones, each sensitive to different wavelengths of light and these are:

- **S-cones** (short wavelength) Blue
- **M-cones** (medium wavelength) Green
- **L-cones** (long wavelength) Red

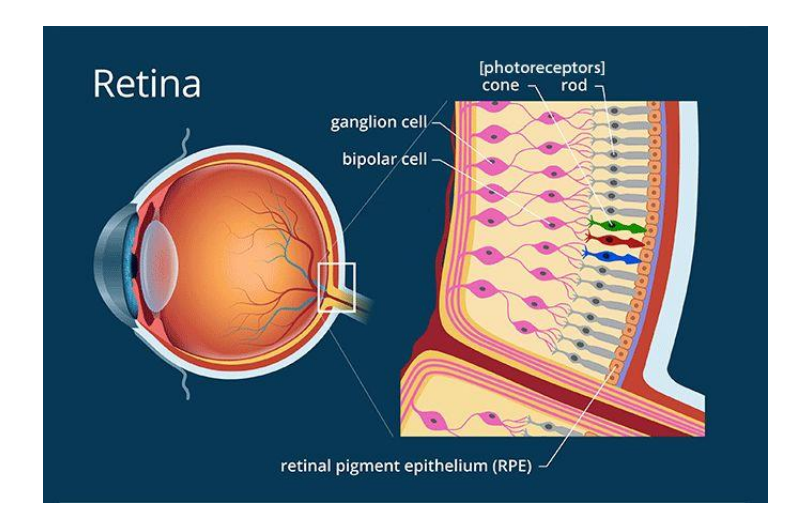


Figure 1.2: Photo of the retina showing rods and cones

The human retina is made up of ten layers, each with specialized structures and optical properties that influence how light propagates through it. These layers vary in thickness and refractive indices. The differences in refractive indices between layers result in partial reflections of light, which are essential for imaging techniques like Optical Coherence Tomography (OCT).

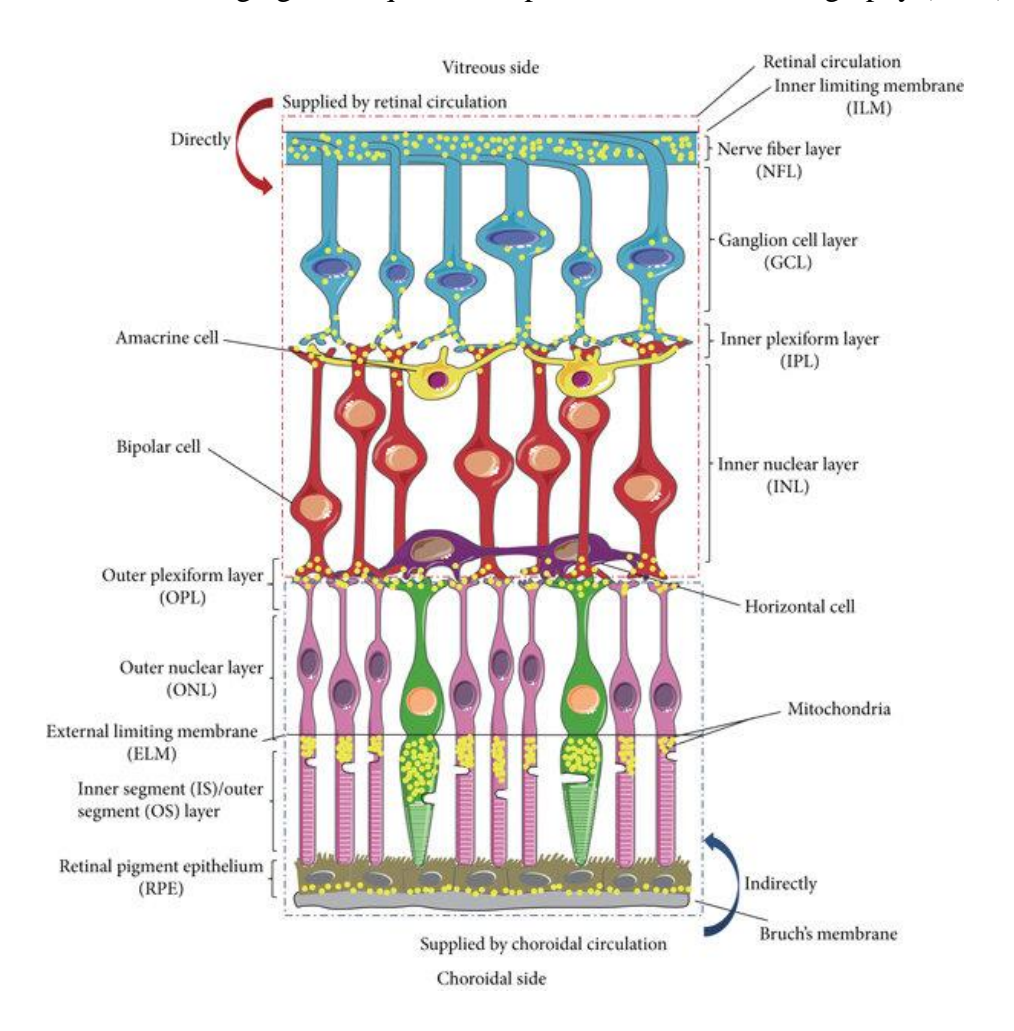


Figure 1.3: Layers of the retina

The table below summarizes the typical thickness and refractive index of each major retinal layer in order from the innermost layers closer to the pupil to the layers further towards the posterior and periphery of the eyeball.

Name of the layer	Approximate Thickness (µm)	Approximate Refractive index (n)
1. Inner Limiting Membrane (ILM)	~2 to 3	~1.35 to 1.38
2. Retinal Nerve Fiber Layer (RNFL)	~10 to 30	~1.38 to 1.41
3. Ganglion Cell Layer (GCL)	~10 to 20	~1.36 to 1.38
4. Inner Plexiform Layer (IPL)	~20 to 40	~1.36 to 1.38
5. Inner Nuclear Layer (INL)	~20 to 40	~1.36 to 1.38
6. Outer Plexiform Layer (OPL)	~20 to 30	~1.36 to 1.38
7. Outer Nuclear Layer (ONL)	~30 to 50	~1.36 to 1.38
8. External Limiting Membrane (ELM)	~2 to 4	~1.36 to 1.38
9. Photoreceptor Layer	~30 to 50	~1.38 to 1.41
10. Retinal Pigment Epithelium (RPE)	~10 to 14	~1.36 to 1.38

Table 1.1: Retinal layers with their corresponding thickness and refractive indices.

Whenever light encounters a boundary between two media of different refractive indices, partial reflection occurs. The amount of light reflected versus that transmitted is described by Fresnel's equation. For normal incidence, the reflectance R is:

$$R = \left(\frac{n_1 - n_2}{n_1 + n_2}\right)^2$$

In order to produce intricate structural maps that allow for the visualization of retinal layers and abnormalities, OCT depends on these faint backscattered signals from several retinal interfaces. These reflections due to variations in refractive indices between the layers, enable the differentiation of each layer based on the strength and timing of the reflected light. An accurate understanding of these refractive indices is necessary not only for creating contrast between layers but also for converting optical path lengths into physical distances, which is critical for accurately measuring retinal thickness.

Abnormalities in reflection patterns or layer thickness, such as thinning of the retinal nerve fiber layer or disruption at the photoreceptor-RPE interface are early warning signs of conditions like glaucoma, macular degeneration, or diabetic retinopathy. For OCT to be effective in identifying and tracking retinal diseases, it is essential to comprehend and make use of refractive index differences.

1.3 General terms related to light

• Refraction

Refraction is the bending of a wave passing from one medium to another. If a medium has a higher refractive index, light slows down more and bends more toward the normal when entering that medium.

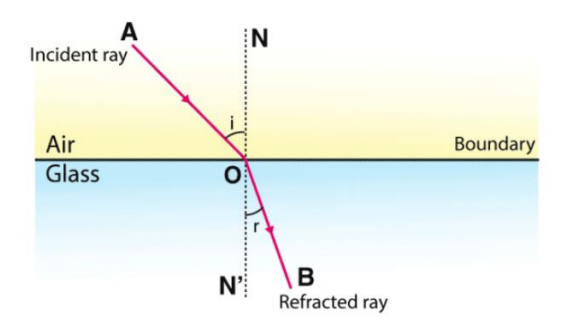


Figure 1.4: Refraction of light

We can calculate how much the light will bend using Snell's law;

$$n_1 sin\theta_1 = n_2 sin\theta_2$$

Where:

 n_1 is the refractive index of the first medium

 n_2 is the refractive index of the second medium

 θ_1 is the angle of incidence

 θ_2 is the angle of refraction

• <u>Diffraction</u>

Diffraction is the phenomenon where light bends around obstacles or spreads out when passing through small openings.

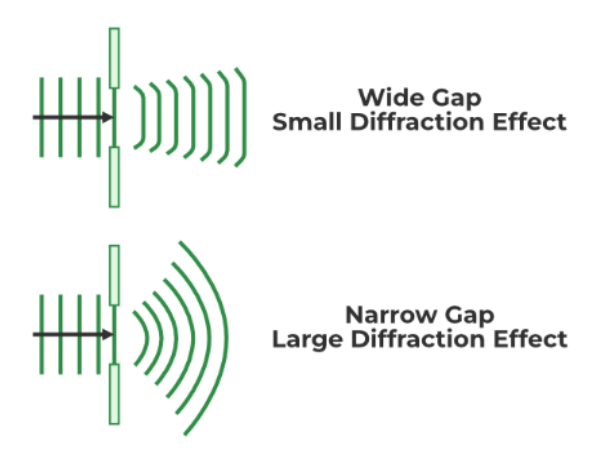


Figure 1.5: Diffraction of light

1.3.1 Young's double-slit experiment

In 1801, Thomas Young performed an experiment that demonstrated interference of light and explained the phenomenon as proof of light's wave nature.

In Young's experiment, a coherent light source, such as a laser, is directed toward two closely spaced, narrow slits (s1 and s2). When the light passes through the slits, it diffracts and the two emerging wave fronts overlap and interfere on a screen placed behind the slits. The resulting pattern of alternating bright and dark bands seen on the screen is known as interference fringes. The bright fringes represent constructive interference and the dark fringes, destructive interference.

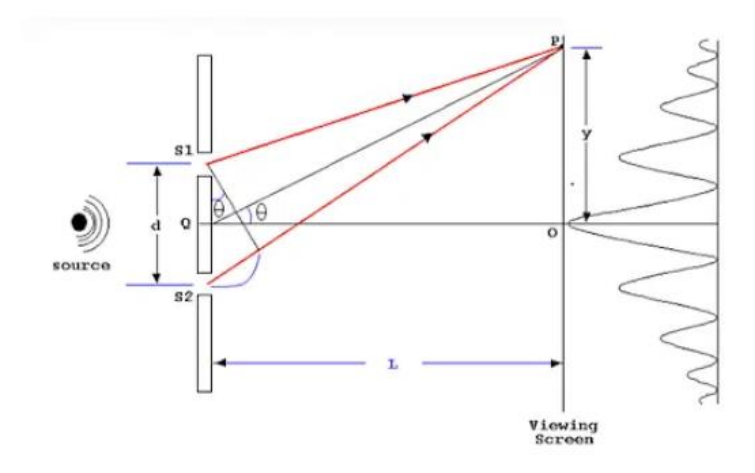


Figure 1.6: Young's double slit experiment

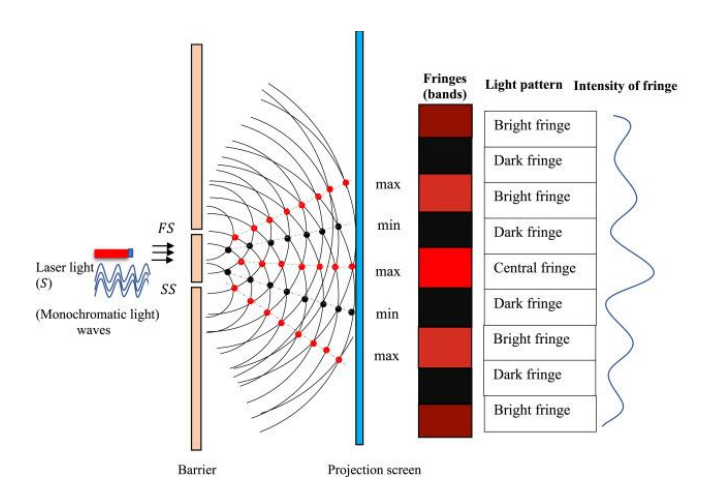


Figure 1.7: Fringes on the screen from Young's double slit experiment. Reproduced from [18]

Bright fringes (constructive interference) occur when $dsin\theta = m\lambda$

Dark fringes (destructive interference) occur when $dsin\theta = (m + \frac{1}{2}\lambda)$

1.3.2 Calculating the intensity of fringes in Young's double-slit experiment

The distance between two adjacent bright (or dark) fringes is called the fringe width (β)

$$\beta = \frac{\lambda L}{d}$$

Where:

- L is the distance from the slits to the screen
- *d* is the distance between the slits

The intensity at any point in the screen depends on the phase difference ϕ of the two light waves from the slits. The intensity is maximum at the center (central fringe)

If the amplitudes od waves from both slits are equal and the maximum intensity at the center is I_0 , the intensity at a point with phase difference ϕ is;

$$I = I_0 cos^2 \left(\frac{\phi}{2}\right)$$

$$\phi = \frac{2\pi}{\lambda} \Delta x$$

Where:

- I_0 is the maximum intensity (at the central bright fringe)
- ϕ is the phase difference and depends on the path difference Δx

1.4 <u>Interference of light</u>

Interference of light is a phenomenon that occurs when two light waves travelling in the same medium are superimposed resulting in the redistribution of light intensity. The resulting intensity depends on the path length difference

Conditions for interference of light

- 1. The waves should originate from coherent sources
- 2. The waves must have the same direction of propagation
- 3. The waves should be polarized in the same direction
- 4. The waves must have the same direction of vibration so that vector quantities can be practically considered as carried by the same axis and added algebraically

When two waves interfere at a point, the phase difference $\Delta \varphi$ between the latter is given by;

 $\Delta \varphi = 2\pi x \frac{(t_2 - t_1)}{T}$

Where: t_1 is the delay of the first wave (s)

• t_2 is the delay in the second wave (s)

• T is the period common to the 2 waves

• $\Delta \varphi$ is the phase shift (rad)

There are two types of interference:

• Constructive interference

• Destructive interference

1.4.1 <u>Constructive interference</u>

The constructive interference occurs when a crest of one wave meets a crest of another wave of the same frequency, then the resultant amplitude is the sum of the individual amplitudes of the waves. Constructive interference occurs when the phase difference ($\Delta \varphi$) between the waves is an even multiple of (π). This happens when the path length difference (ΔL) between the waves is an integer multiple of the wavelength. Constructive interference produces bright fringes

$$\Delta \varphi = 2m\pi$$

$$\Delta L = m\lambda$$

Where: m=0,1,2...

13

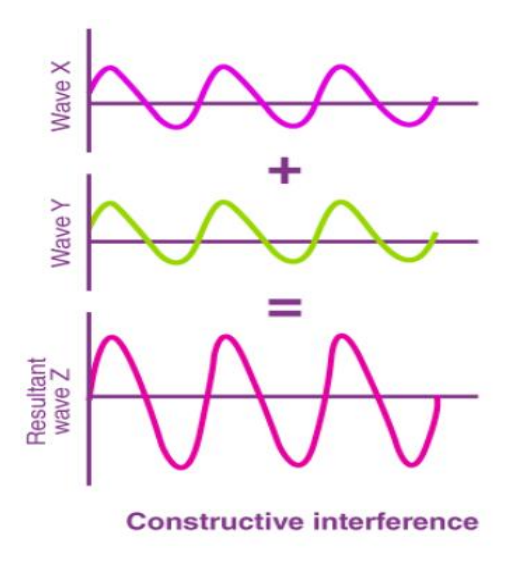


Figure 1.8: Constructive interference

1.4.2 <u>Destructive interference</u>

Destructive interference takes place within the medium when the two waves that interfere with

each other have a displacement in the opposite direction. When a crest of a wave meets a trough of another wave, the waves are said to undergo destructive interference. The resulting amplitude of the wave, which undergoes destructive interference, is equal to the difference in the individual amplitudes of the waves. This type of interference occurs when the phase difference is an odd multiple of π . Destructive interference produces dark fringes.

$$\Delta \varphi = (2m+1)\pi$$

$$\Delta L = (m + \frac{1}{2})\lambda$$

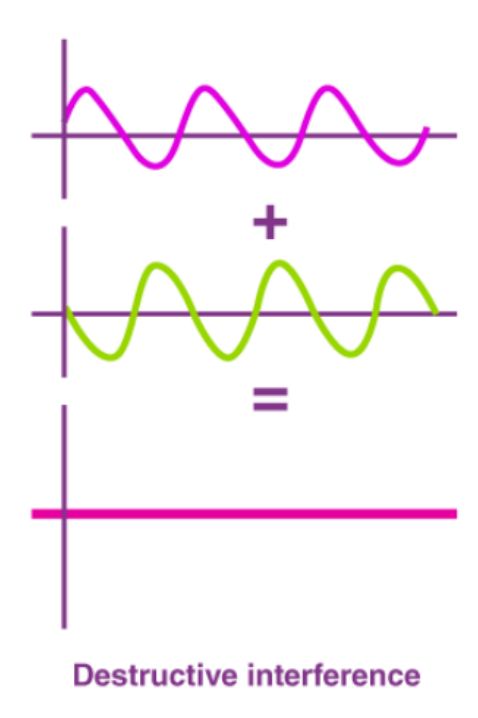


Figure 1.9: Destructive interference

Note:

In reality, it is difficult to obtain interference from two different sources of light. Instead, secondary light sources which will produce waves that will interfere are created from one principle source. This idea gave birth to two principals for the creation of interference and these are;

1. <u>Interference by wave front division</u>

This kind of interference occurs when a single wave front is divided into 2 or more parts using optical elements like mirrors, slits or lenses. These parts travel different paths before overlapping to produce interference patterns.

This principal is commonly used where a single coherent light source is divided to create 2 or more mutually coherent beams.

2. <u>Interference by amplitude division</u>

This interference occurs when a single light wave is partially reflected and transmitted at an optical boundary creating multiple coherent wave fronts. The wave fronts travel in different paths and recombine to form interference patterns

1.5 Coherence

Coherence of light refers to the ability of light waves to maintain a fixed phase relationship over time and space. There are two types of coherence;

- Temporal coherence
- Spatial coherence

1.5.1 Temporal coherence

Temporal coherence describes how well a wave maintains a stable phase relationship over time at a single point in space. It is fundamentally linked to the spectral bandwidth of the light source. Light sources with narrow spectral bandwidths (highly monochromatic light, like lasers) exhibit high temporal coherence. In contrast, broadband sources such as white light emit a mix of wavelengths, leading to low temporal coherence. Temporal coherence is quantified using coherence time and coherence length.

Coherence time (τ_c) is the period over which the phase of a light wave remains predicable and coherence length (L_c) is the distance within this time

$$\tau_c = \frac{L_c}{c}$$

Coherence length and coherence time are critical parameters that determine the visibility and stability of interference fringes. The coherence length is the maximum path difference over which two light waves can interfere constructively or destructively. If the optical path difference

between interfering beams is greater the coherence length, the waves become uncorrelated, and interference fringes disappear.

Light sources with longer coherence, like lasers, can sustain interference over longer periods of time and farther distances, enabling accurate measurements and distinct fringe patterns. On the other hand, light from broadband sources, such as white light or LEDs, has a short coherence time and can only cause interference when the path difference is very small.

1.5.2 **Spatial coherence**

Spatial coherence is the correlation of the phase of a wave at different points across a wave front. It quantifies the ability of light waves at separate points in space to interfere with each other. A point-like or collimated light source, like a laser, with smooth, well-defined wave fronts is usually used to achieve high spatial coherence. Extended or incoherent sources, such as lamps or LEDs, emit light from numerous uncorrelated points, resulting in low spatial coherence. High spatial coherence enables the formation of clear and stable interference patterns while low spatial coherence cause interference fringes to blur or disappear.

In spatial coherence, the coherence area (A_c) is the area over which the light field maintains a fixed phase relationship.

$$A_c \approx \left(\frac{\lambda}{\theta}\right)^2$$

$$L_c = \frac{\lambda R}{D}$$

Where λ is wave length of light wave

- θ is angular size of the source
- R is the distance from the source
- *D* is the source diameter

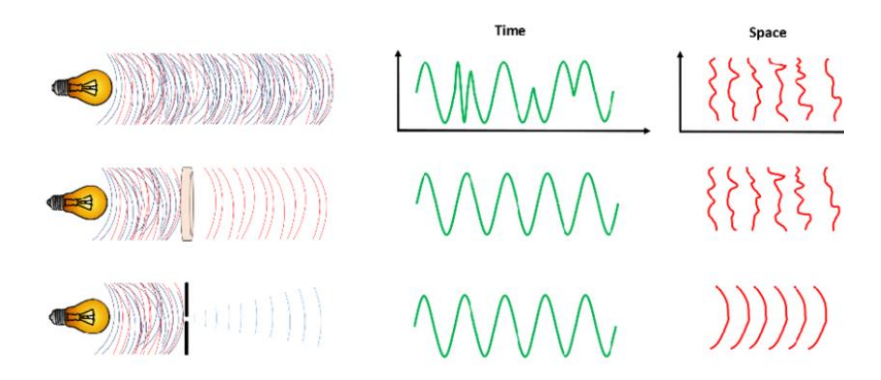


Figure 1.10: Spatial and temporal coherence

1.6 Interferometry

Interferometry is a technique which uses the interference of superimposed wave to extract information e.g. distance, surface irregularities, refractive indices and more. This process is carried out using an interferometer. It involves splitting a coherent wave (like a laser beam) into two or more paths using a beam splitter. These paths may traverse different distances or interact with different materials before being recombined.

Types of interferometers

There are many different interferometers and these include;

- Twyman-Green Interferometer
- Michelson Interferometer
- Mach–Zehnder Interferometer
- Fabry–Pérot Interferometer
- Fizeau Interferometer
- Sagnac Interferometer
- Jamin Interferometer
- Rayleigh Interferometer
- Linnik Interferometer

• Dual Frequency Laser Interferometer

For the purpose of our research, we shall be focusing on the Michelson interferometer.

1.6.1 <u>Michelson interferometer</u>

The Michelson interferometer is a highly precise optical instrument used to measure wavelengths, small distance changes, and refractive index variations.

The Michelson interferometer works based on the principle of constructive and destructive interference of light waves. It splits a monochromatic light beam into two perpendicular beams, reflects them back using mirrors, and recombines them to produce an interference pattern.

Components of the Michelson interferometer

- 1. A monochromatic and coherent light source e.g. laser
- 2. Beam splitter
- 3. Mirrors
- 4. Detector, screen
- 5. Compensator plate (optional)

1.6.2 Principle of Operation of the Michelson interferometer

The light from a monochromatic source strikes the beam splitter, which is a half-silvered mirror. The beam splitter splits the incident light into two beams of equal intensity at a 90° angle. One beam is reflected towards mirror 1(M1) and the other is transmitted toward mirror 2 (M2). The two mirrors are placed perpendicular to each other. Mirror 2 (M2) is fixed, while mirror 1 (M1) is movable to create a path difference.

The Michelson interferometer thus has two arms; the reference arm(M1) and sample arm (M2). Reflection takes place from the mirrors and the two beams reflect off M1 and M2 and travel back toward the beam splitter. When the beams recombine at the beam splitter, they interfere constructively or destructively, depending on the path difference. An interference pattern appears as bright and dark fringes on the screen, only if optical path lengths of both beams is within the

coherence length of the light source. The intensity of the light at the detector (screen) depends on the reflectivity and optical path length of both interferometer arms

A compensator plate, made of the same material and has the same thickness as the beam splitter, is sometimes placed in the transmitted beam path to balance the optical path length

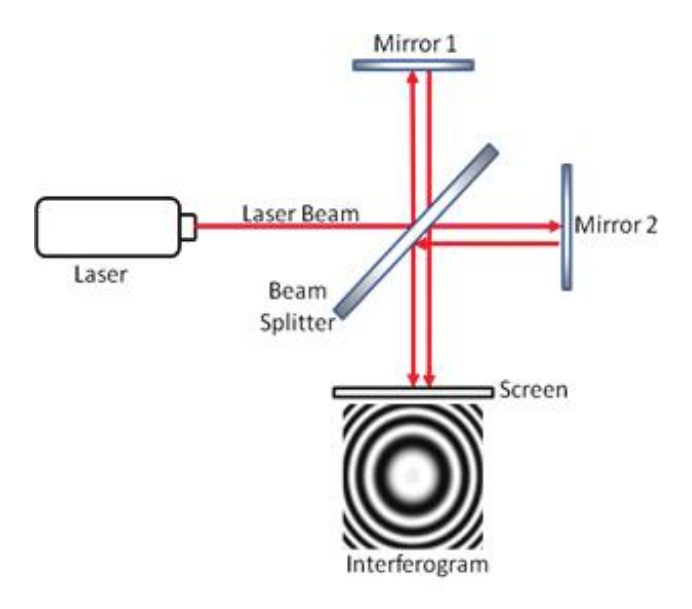


Figure 1.11: Michelson interferometer

1.6.3 Path Difference & Fringe Formation

Path difference ΔL is the difference in optical path lengths and is given as;

$$\Delta L = 2(L_2 - L_1)$$

Where L_1 and L_2 is the distance from the beam splitter to mirror 1 and mirror 2 respectively.

If the optical path difference is an integer multiple of the wavelength (λ) , constructive interference occurs (bright fringe).

$$\Delta L = m\lambda$$

If the optical path difference is an odd multiple of $\lambda/2$, destructive interference occurs (dark fringe).

$$\Delta L = (m + \frac{1}{2})\lambda$$

where m is an integer.

1.6.4 Coherence length

The interferometric signal can be characterized either by its coherence time τ_c or by its coherence length l_c . The coherence length describes the ability of the system to separate different interference reflections from each other.

$$\tau_c = \frac{4ln2}{\pi \Delta v}$$

$$l_c = c\tau_c = \frac{4ln2}{\pi} \frac{\lambda_0}{\Delta \lambda}$$
 with $\Delta \lambda = \lambda_0^2 \frac{\Delta v}{c}$

1.6.5 Calculation of light intensity detected

• Electric field representation

The amplitudes of the electric fields resulting from the reflection on the mirrors of the reference arm and the sample can be written as;

$$\vec{E}_r(t - \frac{L_r}{c})$$

$$\vec{E}_s(t - \frac{L_{so}}{c}) \tag{1.1}$$

Where L_r and L_{s0} are the optical paths of the reference and sample arms respectively.

• Optical delay

The optical delay τ is then defined from the optical path difference ΔL :

$$\tau = \frac{\Delta L}{c} = \frac{L_S - L_r}{c} = \frac{2n_0}{c} (I_{s0} - I_r)$$
 (1.2)

Where $n_0=1$ is the refractive index of vacuum, c the speed of light in a vacuum.

Intensity at the detector

The light intensity at the detector is the time-averaged square of the sum of the fields and can be expressed in the form;

$$I_d(\tau) = \langle [\vec{E}_S(t) + \vec{E}_r(t+\tau)]. [\vec{E}_S(t) + \vec{E}_r + (t+\tau)]^* \rangle$$
 (1.3)

Where <> represents the joint average (temporal and spatial) over the integration time (t) which is longer than the oscillation period of the electric fields.

The relation (3) is then written as

$$I = I_r I_s + 2\sqrt{I_r I_s} Re(\gamma(t))$$
(1.4)

Where: $I_s = \langle \vec{E}_s(t) \vec{E}_s^*(t) \rangle$

$$I_{r=\langle\vec{E}_r(t+\tau)+\vec{E}_r^*(t+\tau)\rangle}$$
 (1.5)

 $\Upsilon(\tau)$ is the complex degree of coherence of the electric fields and can be defined by:

$$\gamma(t) = \frac{\langle \vec{E}(t).\vec{E}^*(t+\tau) \rangle}{\langle \vec{E}(t).\vec{E}^*(t) \rangle} \text{ with } 0 \le |\gamma(\tau)| \le 1$$
 (1.6)

 $|\gamma(\tau)|$ ranges from 0 (incoherent) to 1 (coherent)

Y corresponds to the normalized autocorrelation function of the electric field emitted by the light source. According to the Wiener-Khintchine theorem, the complex degree of coherence of the source is the Fourier transform of the spectral density of the source S(v):

$$\gamma(\tau) = \int_{-\infty}^{+\infty} S(v)e^{-i2\pi v\tau}dv \tag{1.7}$$

The signal intensity measured by the detector therefore depends on the shape and spectral width of the light source.

Quasi-chromatic source

In the case of a quasi-monochromatic source of frequency v_0 , the intensity at the detector is written as;

$$I_d(\tau) = I_r + I_s + 2\sqrt{I_r I_s} |\gamma(\tau)| \cos(2\pi v_0 \tau)$$
(1.8)

1.7 Applications of the Michelson interferometer

- 2. It is used in OCT (Optical Coherence Tomography)
- 3. It is a core component of Fourier Transform Infrared Spectroscopy (FTIR)
- 4. Wave length measurement
- 5. Refractive index measurement

1.8 Conclusion

In this chapter, we have explored the foundational principles of optical interference and coherence. These principles form the foundation of advanced optical instruments such as the Michelson interferometer. The Michelson interferometer is the core instrumentation of Optical Coherence Tomography (OCT). OCT provides depth-resolved, micrometer-scale retinal imaging by combining this interferometric architecture with low-coherence light.

As part of our project, the Michelson interferometer is used as the basis for designing a new version, which will then be simulated using the COMSOL software.

2. OCT and Digital Micromirrors

2.1. <u>Introduction</u>

Optical Coherence Tomography (OCT) is an imaging technique that generates high-resolution, cross-sectional images of biological tissues in a non-invasive manner. Its applications include ophthalmology and dermatology to material inspection and industrial metrology. The principle of OCT is based on low-coherence interferometry, which is implemented using a Michelson interferometer configuration.

The need for improved spatial resolution and faster acquisition speeds has motivated researchers to investigate new approaches to parallelizing OCT signal processing and detection like the integration of MEMS Digital Micromirrors into OCT.

This chapter presents a detailed exploration of OCT fundamentals, digital micromirrors and their role in enhancing OCT performance

2.2. Optical Coherence Tomography (OCT)

Optical Coherence Tomography (OCT) is a non-invasive imaging technique which uses light waves to capture high-resolution, cross-sectional (2D) and volumetric (3D) images of biological tissues. It enables sub-surface images of translucent or opaque materials to be obtained at a resolution equivalent to that of a low-power microscope. It is comprehensively used by ophthalmologists and optometrists but is also used in cardiology, dermatology, oncology, and industrial inspection.

OCT is similar to ultrasound imaging, but instead of sound waves, it uses low-coherence light to measure the echo time delay of backscattered or reflected light from different layers within the tissue. It is thus based on the optical contrast provided by the inhomogeneities in the refractive indices of the different elements of the medium

The principle of OCT is therefore to eliminate multi-scattered photons and detect ballistic photons, which are retroreflected by structures and do not undergo any scattering in the medium.

OCT works based on the principle of low-coherence interferometry.

2.2.1 Principle of low-coherence interferometry

The core of low-coherence interferometry instrumentation is the Michelson interferometer. A low-coherence light source (e.g. super luminescent diodes or femtosecond lasers) emits light which is split into two directions by a beam splitter that form the two interferometer arms.

In the reference arm, the light is reflected back by the reference mirror, while in the sample arm, the light is reflected back by the sample under test (biological tissue).

The reflected light from both arms is recombined at the beam splitter and an interference pattern is formed on the photodetector. Due to the coherence properties of the light, an interference pattern is formed only when the optical path lengths of both arms match within the coherence length of the source. The photodetector measures the intensity of light resulting from the interference. The depth-resolved information obtained from the interference signal forms the basis of OCT imaging techniques.

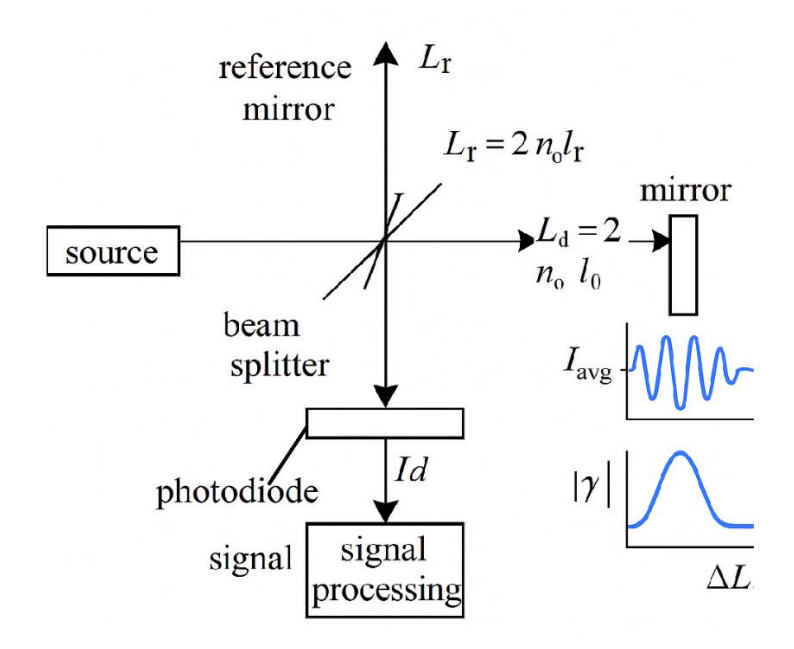


Figure 2.1: Low-Coherence interferometer. Reproduced from [17]

 I_d is the intensity detected by the photodiode.

 $|\gamma|$ is the real envelope of the signal.

The depth displacement is achieved by moving the reference mirror at a constant speed V_m .

2.2.2 Intensity of light on the photodiode in OCT

From equation (1.8) of the intensity I_d detected on the screen in a Michelson interferometer, it can be noted that I_{OCT} is the sinusoidal component of I_d .

$$I_d(\tau) = \underbrace{I_r I_s}_{I_{moy}} + \underbrace{2\sqrt{I_r I_s} |\gamma(\tau)| \cos(2\pi v_0 \tau)}_{I_{OCT}}$$
(2.1)

If the spectral profile of this source is Gaussian (case of super luminescent diodes), the complex degree of coherence is written as:

$$\gamma(t) = e^{-\left(\frac{\pi\Delta v\tau}{2\sqrt{\ln 2}}\right)^2} e^{-i2\pi v_0 \tau} \tag{2.2}$$

Where v_0 is the frequency at which the power spectral density has a maximum and Δv is the spectral width FWHM (Full Width at Half Maximum), defined at half-height.

We can thus observe that:

- The larger the spectral width of the source Δv , the narrower the envelope of the complex degree of coherence.
- The amplitude of the interference term I_{OCT} decreases with increasing delay τ along the two arms of the interferometer.

It is also possible to rewrite I_{OCT} as a function of the optical path difference. We then obtain

$$I_{OCT}(\Delta L) = 2\sqrt{I_r I_s} |\Upsilon \Delta L| cos\left(\frac{2\pi}{\lambda_0} \Delta L\right)$$
 (2.3)

Where λ_0 corresponds to the average wavelength of the source

The interferometer shown in Figure 2.1 can be used for deep imaging of biological tissues by modulating the signal from the reference arm.

2.2.3 **Depth Movement**

When the reference mirror is moved at a constant speed V_m , the optical path difference between the two arms is modified as follows:

$$\Delta L(t) = \Delta L_0 + 2V_m t \tag{2.4}$$

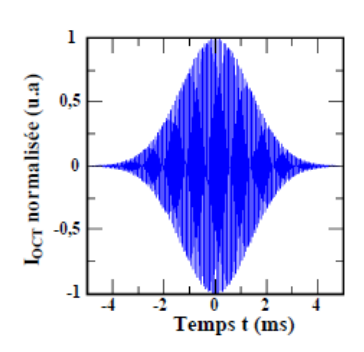
Where ΔL_0 is the optical path difference when the two arms are at rest. If a mirror is placed in the sample arm, the interferometric signal (2.3) can then be written as;

$$I_{OCT}(t) = 2\sqrt{I_r I_s} \left| \Upsilon(\Delta L_0 + 2V_m t) \right| \cos\left(\frac{2\pi}{\lambda_0} \Delta L_0 + 2\pi f_0 t\right)$$
(2.5)

Where f_0 is the modulation frequency of the OCT signal such that;

$$f_0 = \frac{2V_m}{\lambda_0} \tag{2.6}$$

2.2.4 Processing an OCT signal



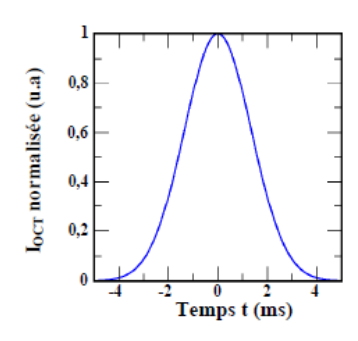


Figure 2.2: OCT signal before processing. Figure 2.3 OCT signal after processing. Reproduced from [17]

Reproduced from [17]

Once the interferometric signal (I_d) has been detected by the photodiode(detector), it must be processed in order to recover only the envelope associated with the degree of coherence (|Y|).

The OCT signal in figure 2.3 has been treated by band-pass filtering around the modulation frequency.

2.2.5 Stratified medium

If the mirror in the sample arm of the low coherence interferometer (figure 2.1), is replaced by a weakly scattering biological tissue e.g. the eye, the interferometric signal (I_d) detected by the photodiode is then more complex.

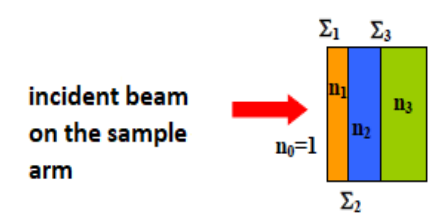


Figure 2.4: Stratified medium composed of 3 layers with different refractive indices. Reproduced from [17]

Since the layers have different refractive indices, the interferometric signal detected when demodulated is composed of three peaks. These peaks correspond to the interfaces $\Sigma 1$, $\Sigma 2$ and $\Sigma 3$

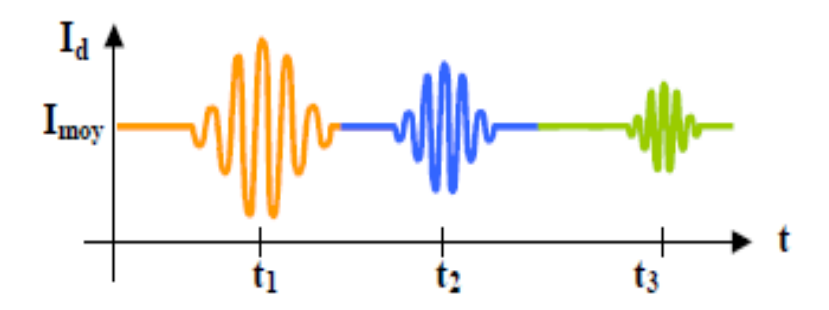


Figure 2.5: Interferometric signal detected on the photodiode when the sample arm has a biological tissue with different refractive indices as shown in figure 2.4.

Reproduced from [17]

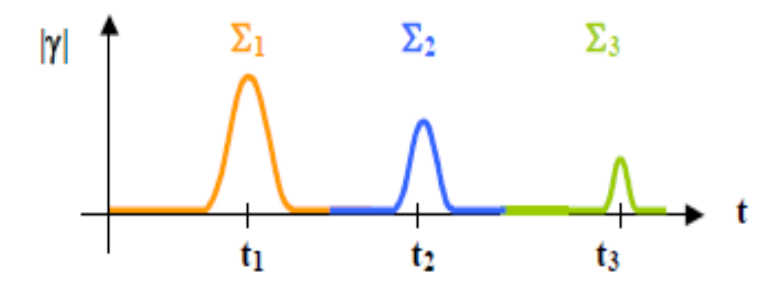


Figure 2.6: Signal after demodulation showing 3 peaks corresponding to the 3 interfaces. Reproduced from [17]

2.2.6 Scanning modes in OCT

OCT uses different scanning modes to capture detailed information from different regions of the sample. These modes differ based on how the optical beam is directed across the tissue and how the backscattered signals are collected.

OCT scanning is collinear i.e. the emitted and reflected light signals travel along the same axis, enabling the measurement of surfaces with sharp edges and channels.

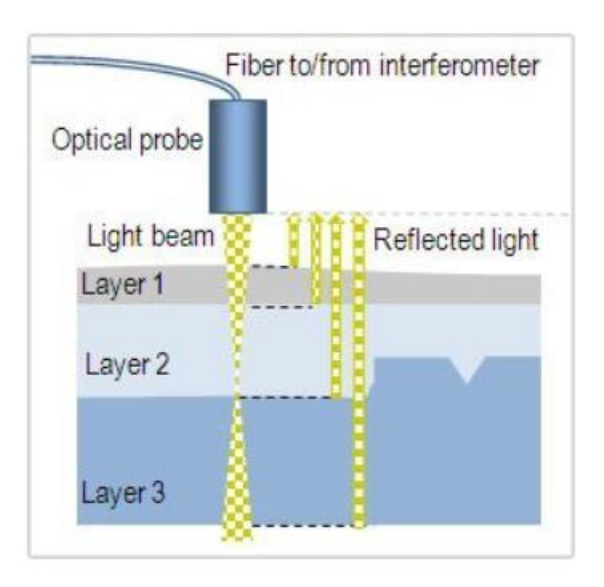


Figure 2.7: Low-coherence beam scanning through multilayer sample

There are three OCT scanning modes;

- A-scan
- B-scan
- C-scan

a) A-scan

It is a single depth profile (one-dimensional) scan. A-scan can be taken as the abbreviation for axial scan, representing the reflected optical amplitude along a single axis of light propagation. Each A-scan captures the intensity of backscattered light as a function of depth, producing a reflectivity profile of the tissue. Peaks in this profile correspond to interfaces between different tissue layers. These peaks indicate variations in optical properties, allowing for the identification of boundaries. By analyzing these intensity peaks across multiple A-scans, one can delineate smooth and continuous boundaries within the tissue structure. Multiple A-scans are combined to form B-scans.

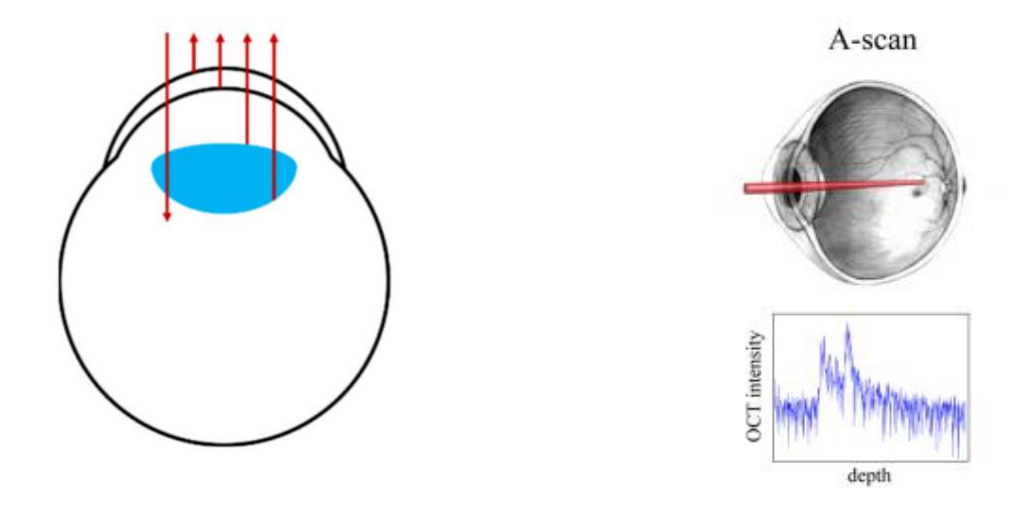


Figure 2.8: A-scan of the eye. Reproduced from [16]

b) <u>B-scan</u>

In ophthalmology, sequence of A-scans across the tissue allows a cross-sectional reconstruction of a plane through the anterior or posterior segment of the eye (biological tissue) producing a two-dimensional image known as a B-scan.

A B-scan represents a cross-sectional image where the amplitudes of backscattered are displayed as a function of depth and lateral position. The resulting images are in either grayscale or false-color scale, where intensity variations correspond to different tissue reflectivities. B-scans provide high-resolution images and are particularly valuable for detailed assessment of the retina. The improved resolution allows subtle fluctuations in reflectivity to be visualized more clearly.

The number of B-scans averaged per frame can be used as an indicator of image quality. The greater the number of B-scans averaged, the higher the image quality. However, increasing the number of scans can slow down the acquisition process and make the data more susceptible to motion artifacts, such as those caused by eye movements.

A B-scan is also referred to as a line scan and can be positioned anywhere across the fundus, including critical areas such as the macula. It provides a cross-sectional view of the retina, allowing visualization of its layered structure and identification of abnormalities such as macular holes, retinal edema or epiretinal membranes.

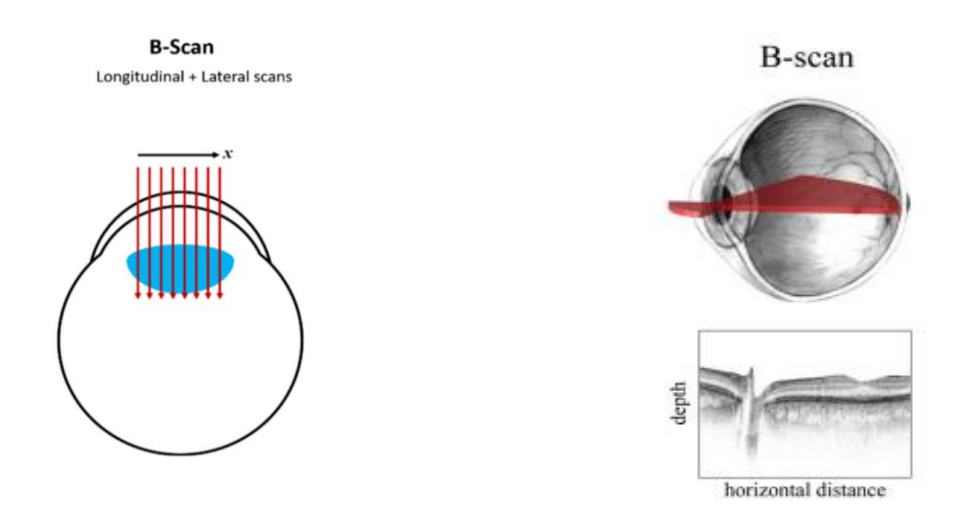


Figure 2.9: B-scan of the eye. Reproduced from [16]

c) <u>C-scan</u>

C-scan refers to a sectional image acquired across structures at a constant optical delay, corresponding to a fixed depth within the tissue. In the eye, the C-scan conveniently aligns with a coronal section, providing a horizontal "slice" through the retinal or choroidal layers. It is a three-dimensional representation generated by stacking multiple B-scans. A C-scan is sometimes referred to as a phase fundus image, as it resembles that of a fundus camera, although it is typically presented in grayscale rather than in color The C-scan derived from OCT, captures information based on the optical reflectivity of tissue layers, enabling better visualization of subtle structural changes at specific depths.

By stacking multiple C-scans at different depths, a three-dimensional volumetric dataset of the tissue can be reconstructed, allowing detailed assessment of retinal diseases layer by layer.

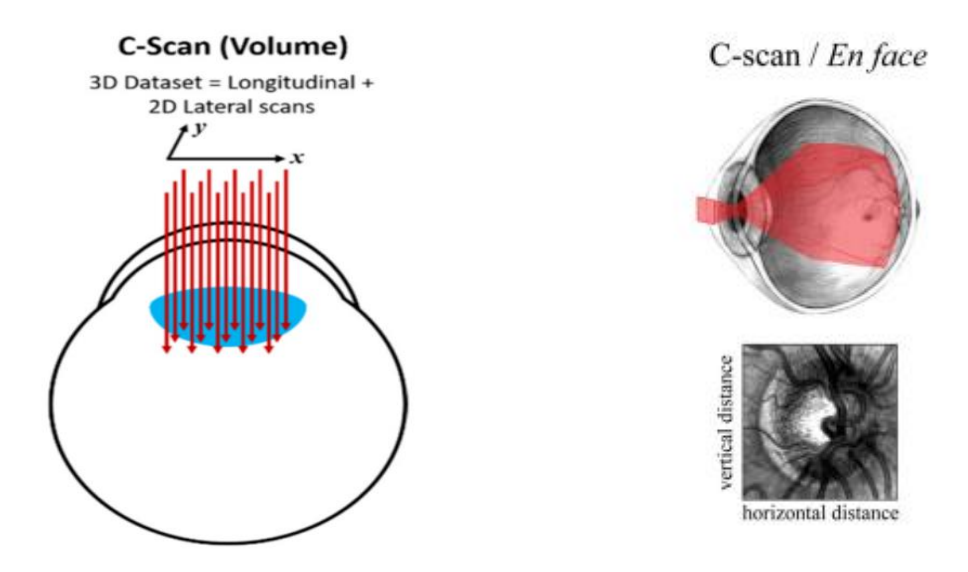


Figure 2.10: C-scan of the eye. Reproduced from [16]

2.2.7 Types of OCT

OCT has evolved into several different types, each optimized for specific imaging needs and clinical applications. OCT systems are categorized based on how they analyze interference signals. Each type brings unique advantages, such as faster image acquisition, improved depth penetration, or higher resolution, making OCT a versatile tool in fields like ophthalmology, cardiology, and biomedical research.

There are two main types of OCT;

- Time-Domain OCT (TD-OCT)
- Fourier-Domain OCT (FD-OCT)

a) <u>Time-Domain OCT</u>

Time-Domain Optical Coherence Tomography (TD-OCT) is the first-generation form of OCT technology, directly adapted from Low-Coherence Interferometry (LCI). In TD-OCT, a low-coherence light source, typically a superluminescent diode (SLD), is split into two paths using a fiber-optic coupler. One path is directed toward the sample under study, while the other is directed toward a movable reference mirror.

The reference mirror in TD-OCT moves mechanically to scan different depths within the sample. As the mirror moves, it changes the optical path difference (OPD) between the sample and reference arms. When the OPD matches, constructive interference occurs, producing an intensity maximum at the detector. This allows the precise localization of reflective structures within the tissue.

The basic setup of TD-OCT typically uses a 2×2 fiber-optic coupler connected to a Michelson interferometer. As the reference mirror scans in position, the detector captures fringe bursts generated when reflections from different tissue depths align with the reference arm's path length. This scanning process builds up depth-resolved information one point at a time.

TD-OCT constructs two-dimensional images by measuring the time delay and magnitude of backscattered light from different depths, in a way similar to ultrasound imaging. However, since only one point is measured at a time and the depth resolution is limited by the coherence length of the light source, the imaging speed is relatively slow compared to newer OCT technologies.

As a result, TD-OCT has largely been replaced by faster and higher-resolution techniques such as Spectral-Domain and Swept-Source OCT in most modern clinical and research application.

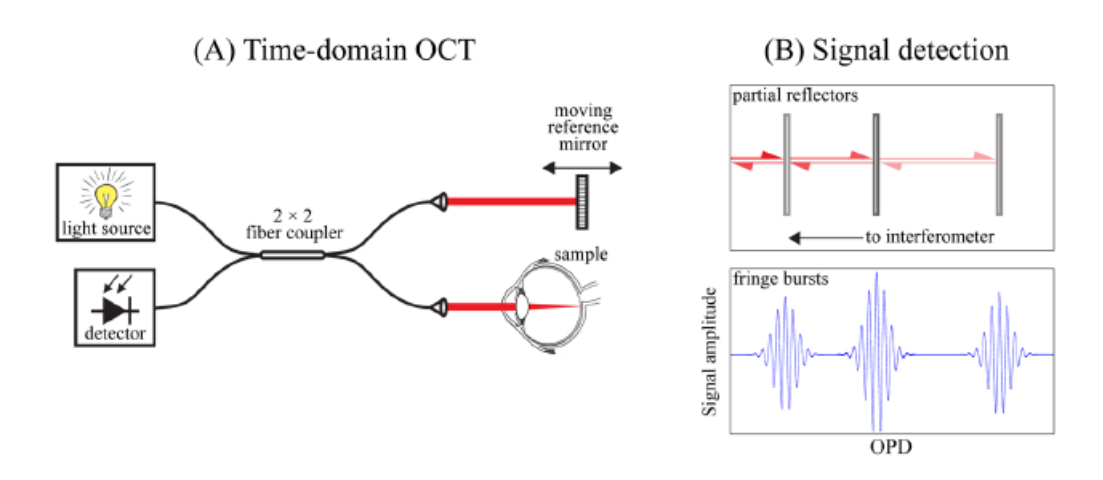


Figure 2.11: Time-Domain OCT. Reproduced from [16]

b) Fourier-Domain OCT

Fourier-Domain Optical Coherence Tomography (FD-OCT) is an advancement over Time-Domain OCT (TD-OCT) that allows much faster and more sensitive imaging by eliminating the need for mechanical movement of the reference mirror. Instead of measuring reflectivity point by point in time, FD-OCT captures the spectral interference pattern and uses a Fourier transform to reconstruct depth information.

FD-OCT can be implemented in two main forms: Spectral-Domain OCT (SD-OCT) and Swept-Source OCT (SS-OCT). Both rely on the same principle of capturing spectral data and converting it into spatial depth profiles, but differ in the way they detect and process the light signal.

FD-OCT systems provide faster image acquisition rates, higher signal-to-noise ratios, and increased sensitivity compared to TD-OCT, making them the preferred method for modern clinical and research applications.

• Spectral-Domain OCT

Spectral-Domain OCT (SD-OCT) is a widely used second-generation OCT technology that captures high-resolution, cross-sectional images without moving the reference mirror. In SD-OCT, a broadband light source, such as a super luminescent diode, is directed at the tissue. The reflected light from the sample and reference arms interferes and is detected by a spectrometer.

The spectrometer includes a diffraction grating and a CCD (Charge-Coupled Device) array that separates the interference signal into different wavelength components. The full spectrum is recorded in a single acquisition, and a Fourier transform is used to reconstruct an A-scan from all depths simultaneously.

SD-OCT enables high-speed acquisition of multiple A-scans to generate detailed B-scans and 3D images. It has become the clinical standard for diagnosing and monitoring conditions like age-related macular degeneration, diabetic retinopathy, and glaucoma.

• Swept Source OCT

Swept-Source OCT (SS-OCT), also known as Optical Frequency Domain Imaging (OFDI), is a third-generation OCT technique that uses a tunable, narrowband laser that rapidly sweeps across a broad spectral range. The interference signal is recorded over time at each wavelength sweep and converted into depth information using Fourier transformation.

Unlike SD-OCT, which uses a spectrometer and CCD, SS-OCT uses a dual-balanced detector and does not require a spectrometer. This configuration allows faster scanning and better suppression of noise, especially from relative intensity fluctuations in the light source.

SS-OCT provides deeper tissue penetration and is particularly effective in visualizing posterior eye structures such as the choroid. Its high imaging speed and wide field-of-view make it ideal for advanced retinal and optic nerve head imaging. SS-OCT is often considered superior to SD-OCT when enhanced depth imaging (EDI) or widefield visualization is needed

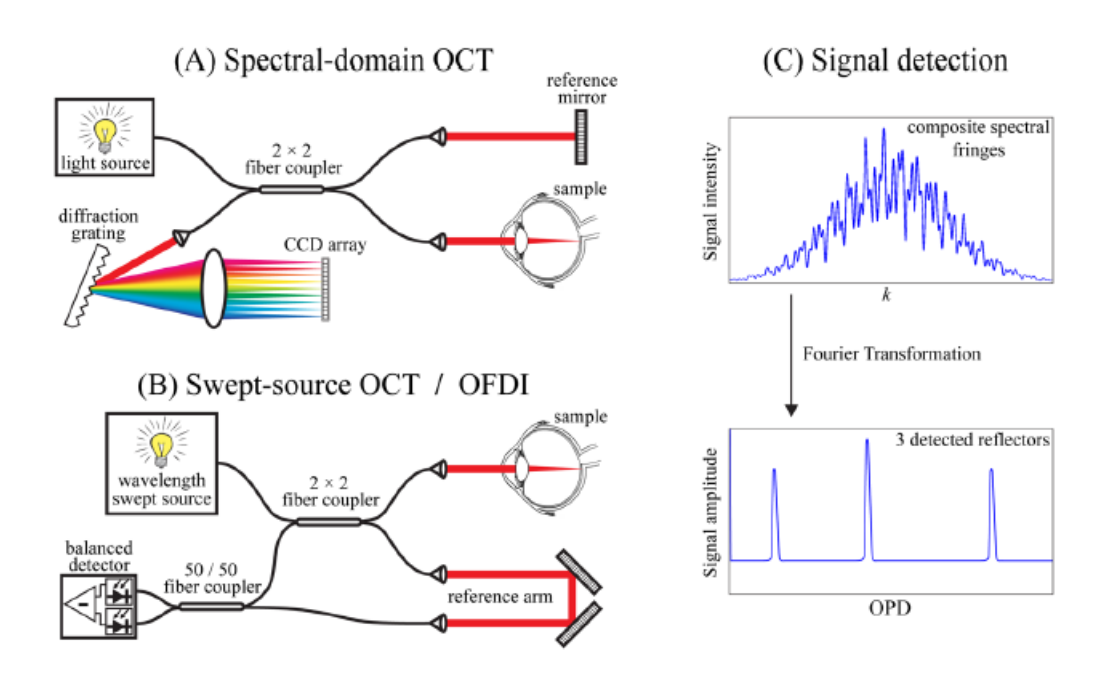


Figure 2.12: Spectral-Domain and Swept-Source OCT. Reproduced from [16]

2.3 <u>Digital Micromirrors</u>

Micromirrors are microelectromechanical systems (MEMS) made of small reflective surfaces that use tiny mechanical movements to precisely manipulate light. They are typically smaller than 1 mm. These mirrors, which can be made as single parts or in arrays, can tilt or move in one or more axes to change the light's intensity or direction. They can be a few micrometers to several hundred micrometers in size. Micromirrors are a crucial component of contemporary optoelectronic systems because they combine optical accuracy with electrical control.

Micromirrors are capable of various types of mechanical movement:

- Tilting (angular movement about one or two axes)
- Piston motion (up-and-down vertical displacement)
- Lateral translation (sideways movement)

Depending on their structure and mounting, micromirrors may be static (fixed position) or dynamic (movable). Dynamic micromirrors are particularly valuable for steering or modulating light beams in real time.

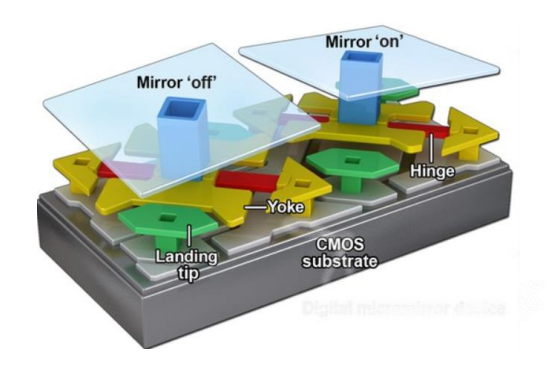


Figure 2.13: Digital micromirror

2.3.1 Structure of micromirrors

Micromirrors often appear as small, square, or circular reflective plates, typically created on silicon substrates by photolithographic and etching processes using materials like polysilicon, aluminum, or gold. These mirror plates are usually supported by mechanical hinges or tethers that allow controlled movement

The hinges are often made from polysilicon or metal layers and allow the mirror to tilt around one or two axes. The hinges also act as torsional springs providing a restoring torque that returns the mirror to its neutral position when an actuation force is removed.

The torsion hinges connect the mirror plate to fixed support posts anchored to the substrate. These posts provide mechanical stability and electrical isolation between the movable mirror and the substrate.

Some advanced micromirror designs may include multiple electrodes to allow bi-directional or multi-axis tilting, enabling more complex and programmable control of the mirror orientation.

This structure allows micromirrors to function with high speed, low power consumption, and precise angular control, making them ideal for applications such as beam steering, projection systems, and optical coherence tomography (OCT).

2.3.2 Types of micromirrors

Micromirrors are categorized based on their degrees of freedom, motion type, and actuation method. There are four main categories of micromirrors and these are:

a) Electrostatic Micromirrors

Electrostatic micromirrors are MEMS devices that utilize electrostatic forces to induce controlled tilting or displacement of micro-scale reflective mirrors. The mirror plate and fixed electrode form a parallel-plate capacitor. By applying a voltage between the mirror and underlying or adjacent electrodes, an attractive force is generated. The mirror tilts until the electrostatic force balances the mechanical restoring torque from the suspension. In the ON state, a voltage is applied, generating an electrostatic force that causes the mirror to tilt to a predefined angle (e.g., $+12^{\circ}$ or -12° , depending on the design). In the OFF state, the voltage is removed, and the torsional restoring force brings the mirror back to its neutral, flat position.

b) Piezoelectric micromirrors

Piezoelectric micromirrors are MEMS devices that use the piezoelectric effect to achieve precise, high-speed mechanical motion. These devices convert electrical signals into mechanical deformation via piezoelectric materials, enabling efficient and fast actuation with relatively low voltage and power consumption.

When a voltage is applied across the piezoelectric layer, it causes it to expand or contract due to the inverse piezoelectric effect. The strain mismatch between the piezoelectric layer and the elastic substrate (e.g., silicon or SiO2) causes bending of the actuator beam (unimorph or bimorph structure). The bending motion is transferred to the mirror plate, causing it to tilt (tiptilt) or move piston-like (out-of-plane translation). By controlling voltage polarity and magnitude on different actuator groups, multi-axis scanning (two-axis tilt plus piston) is achievable.

c) Electromagnetic micromirrors

Electromagnetic micromirrors are MEMS devices that use electromagnetic forces to tilt or move a tiny reflective mirror for precise optical beam steering. Their actuation principle relies on the Lorentz force generated when an electric current flow through a coil placed in a magnetic field, causing the mirror to rotate. Their structure includes a metallic coil and a permanent magnet. The thin metallic coil is patterned around or on the mirror and it carries the actuation current.

The magnet is positioned beneath or around the mirror chip to provide a static magnetic field perpendicular to the coil.

When an electrical current flow through the coil on the mirror, it interacts with the magnetic field from the permanent magnet. The coil experiences a Lorentz force perpendicular to both the current direction and the magnetic field. This force creates a torque on the mirror, causing it to tilt about the torsion axis. The mirror angle can be precisely controlled by controlling the magnitude and direction of the current

d) Electrothermal micromirrors

Electrothermal micromirrors are MEMS devices that use thermal expansion induced by Joule heating to generate mechanical motion, enabling precise control of mirror tilt (tip-tilt) and piston (out-of-plane) movement. They can produce large angular deflections at relatively low voltages with simple fabrication processes.

Their structure includes electrothermal actuators that are composed of two or more layers of materials with different coefficients of thermal expansion (CTE). When a current is applied through the electrothermal actuator, it causes resistive (Joule) heating. The temperature rise leads to expansion of materials with different CTEs, causing the bimorph beam to bend. This bending translates into angular displacement (tip-tilt) or piston motion of the mirror plate. Precise analog control of mirror position is achieved by controlling current magnitude and distribution.

2.3.3 Applications of digital micromirrors

- They are the core technology in Digital Light Processing (DLP) projectors for cinemas and homes
- Used in real time biomedical imaging and sensing
- Used in wave front shaping to control light propagation through complex media

2.4 <u>Conclusion</u>

Although Optical Coherence Tomography (OCT) offers excellent imaging performance, its real-time use over large areas remains limited. This is mainly due to the sequential data acquisition process, which relies on slow, motion-sensitive mechanical scanning components. These constraints reduce imaging speed, cause artifacts, and compromise optical coherence stability over wide scanning areas, thereby affecting signal quality and resolution.

Our work proposes the integration of digital micromirrors within the Michelson interferometer, the core component of OCT systems, to replace the mechanical elements of the reference arm. This approach enables dynamic redirection of the reference beams, improves coherence stability, reduces system complexity, and allows for real-time parallel acquisition of depth profiles.

Chapter 3:

Design, Implementation and Simulation of a Michelson Interferometer based on Digital Micromirrors

3. <u>Design</u>, <u>Implementation and Simulation of a Michelson Interferometer based on</u> Digital Micromirrors

3.1 Introduction

During the design phase of the Michelson interferometer, we proposed three micromirror-based configurations. In the first configuration, we replaced the beam splitter with a set of micromirrors to direct a single beam, simulating an A-scan acquisition in an Optical Coherence Tomography (OCT) system (Figure 3.1).

The second configuration involved parallelizing the light source of the Michelson interferometer, which constitutes the fundamental element of an OCT system (Figure 3.2).

The third and final configuration replaced the reference mirror with a set of micromirrors to enable parallel acquisition, allowing multiple A-scans to be obtained simultaneously (Figure 3.3).

For this project, we chose to develop and implement the third configuration by designing three acquisition system variants. These variants are similar in concept but differ in the arrangement and number of micromirrors and detectors used.

The modifications focus on the reference arm, which originally contained a fully reflective mirror. In our design, this mirror is replaced by two micromirrors that fulfill the same reflective role

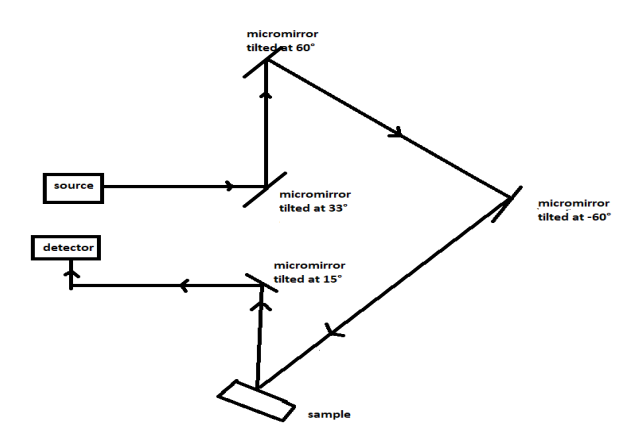


Figure 3.1: Michelson interferometer configuration where the beam splitter is replaced by a set of micromirrors

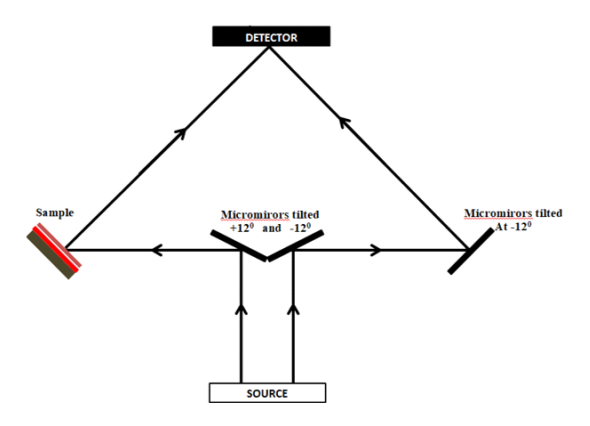


Figure 3.2: Michelson interferometer configuration where the light source is parallelized

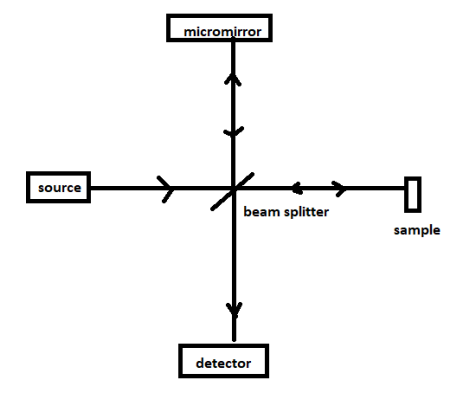


Figure 3.3: Michelson interferometer configuration with micromirrors in the reference arm

3.2 <u>Conceptual Development of Micromirror-Based Michelson Interferometer Configurations</u>

To investigate the integration of digital micromirrors into Michelson interferometers for Optical Coherence Tomography (OCT), we designed and simulated a number of configurations. Each configuration increases the number of rays, micromirrors, and detectors to assess the potential for parallel data acquisition and enhanced imaging speed. The central objective across all designs is to replace conventional static reference mirrors with programmable micromirrors, enabling precise and dynamic control of the optical path in the reference arm.

3.2.1 <u>Single-Beam Michelson Interferometer Configuration with One Micromirror</u>

In this configuration, a light source emits light (one ray) that is directed toward a beam splitter, which divides the beam into two paths: one directed toward a micromirror (the reference arm) and the other toward a sample consisting of four layers with different refractive indices (the sample arm). In this configuration, the micromirror is not tilted to any angle. It is positioned flat at 0°, providing a stable reference path for interference. The micromirror reflects the light back through the beam splitter, and the sample reflects light from each interface between the layers due to changes in refractive index. These reflections travel back toward the beam splitter, where they are recombined with the reference beam. The resulting interference pattern is detected by a photodetector positioned at the output. By adjusting the position or angle of the micromirror, it is possible to vary the reference path length and obtain depth information from the sample. This configuration enables the extraction of axial reflectivity profiles (A-scans), making it a key setup in OCT systems for non-invasive imaging of internal structures.

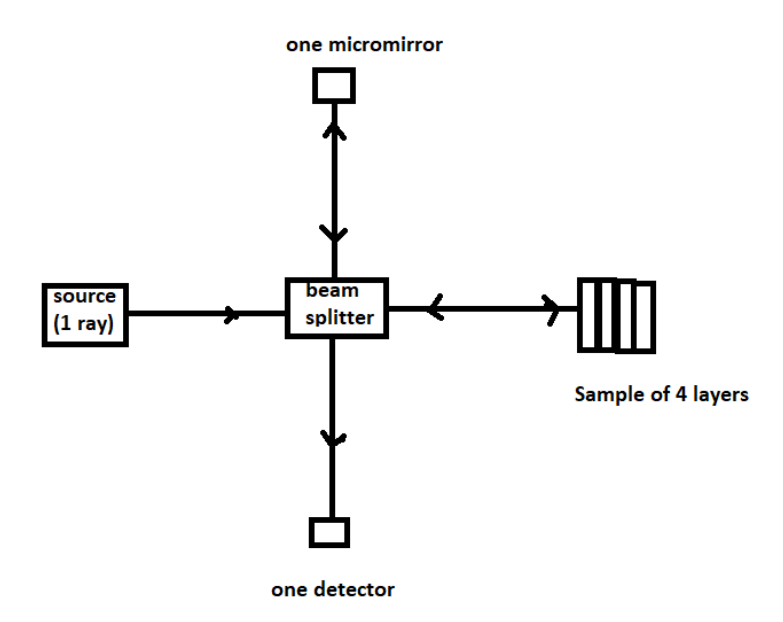


Figure 3.4: Single-beam Michelson interferometer configuration

3.2.2 <u>Dual-Beam Michelson Interferometer Configuration with Two Micromirrors</u>

This Michelson interferometer setup is designed for dual-path interference analysis, commonly applied in advanced OCT systems. In this configuration, a light source emitting two rays simultaneously sends light into a central beam splitter, which divides the rays into two arms. One pair of rays is directed upward toward two independently controlled micromirrors (reference arm), while the other pair is directed rightward toward a sample composed of three layers with varying refractive indices (sample arm). The micromirrors are not tilted to any angle. They are positioned flat at 0°, providing a stable reference path for interference. The light reflects back from both the micromirrors and each interface within the layered sample. These reflected beams are recombined at the beam splitter and directed toward two detectors located at the bottom. Each detector collects interference signals resulting from the optical path length differences between the reference and sample arms. In this setup, the two micromirrors allow independent and simultaneous control of the optical path lengths in the reference arm, enabling the system to probe different depths or regions of the sample at the same time.

The use of two incident beams enables parallel probing of the sample, allowing for simultaneous scans and comparison of different sample regions. Having two detectors enables balanced detection, where signals from both detectors are subtracted to cancel out common noise sources and greatly improve the signal-to-noise ratio, and also allows for the simultaneous collection of data from multiple regions or depths, enhancing sensitivity and efficiency

This dual-detector configuration enhances sensitivity and can allow simultaneous depth profiling or comparison across two regions of the sample. The system provides more detailed structural information and is especially useful when monitoring dynamic changes or implementing parallel OCT measurements.

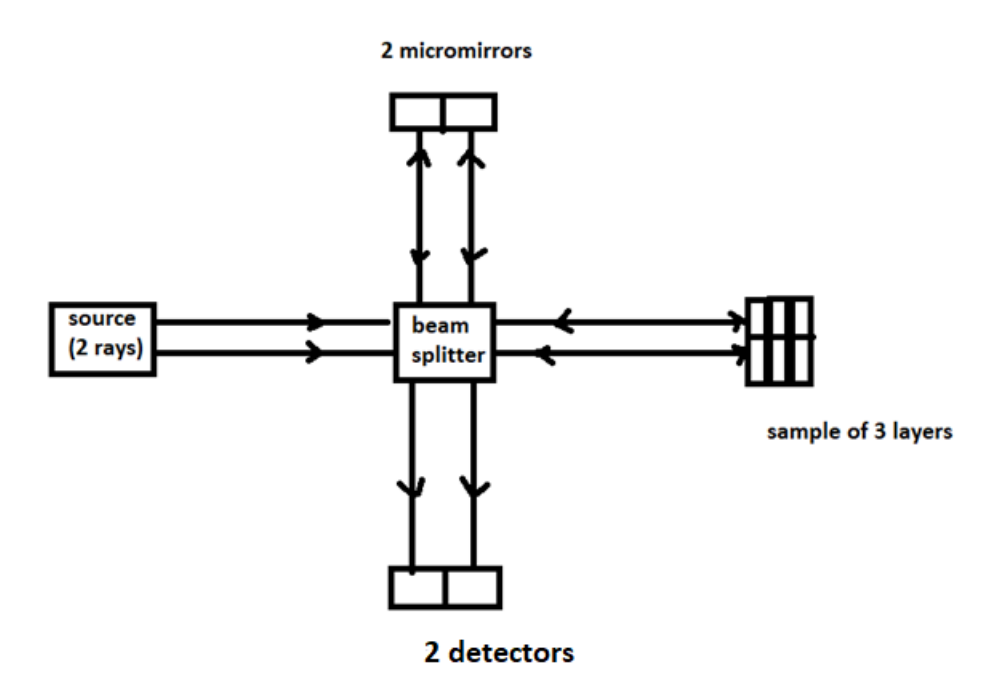


Figure 3.5: Dual-beam Michelson Interferometer Configuration

3.2.3 <u>Dual-Beam Michelson Interferometer Configuration with Two Micromirrors</u>

This Michelson interferometer setup is also designed for dual-path interference analysis, commonly applied in advanced OCT systems. The sample arm is composed of a sample of 4 layers. Its working principle is similar to that of the interferometer described in section 3.1.2.

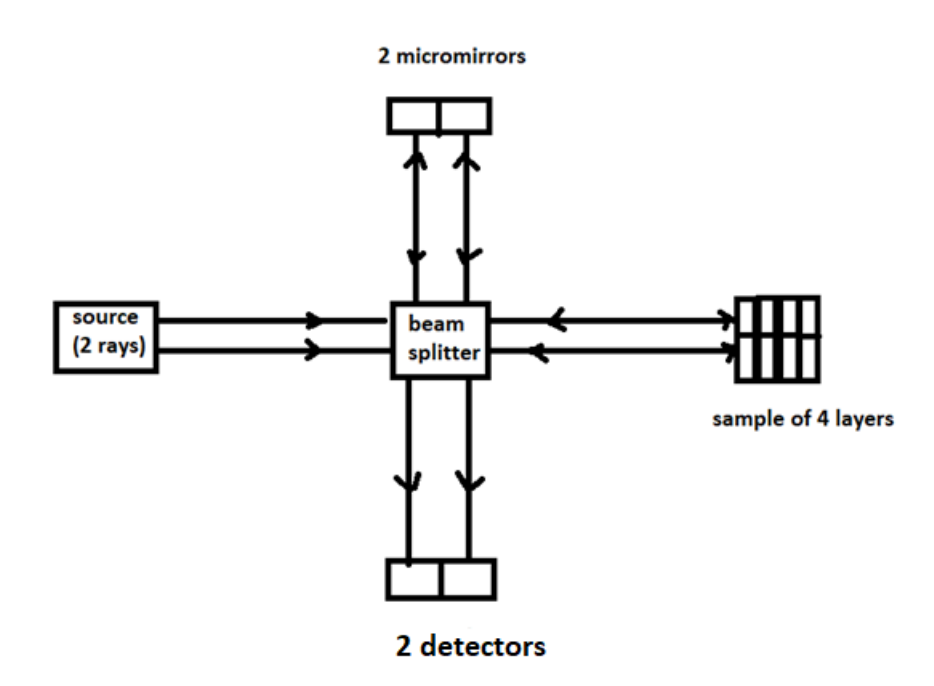


Figure 3.6: Dual-beam Michelson Interferometer Configuration

3.2.4 <u>Triple-Beam Michelson Interferometer Configuration with Three Micromirrors</u>

This Michelson interferometer setup uses a light source that emits three separate rays, each of which is split by a central beam splitter into two paths: one directed upward toward three independently controlled micromirrors (reference arm), and the other directed rightward toward a sample composed of three layers with different refractive indices (sample arm). The micromirrors in this configuration are not tilted to any angle. They are positioned flat at 0°, providing a stable reference path for interference. Each beam strikes the sample at a different lateral position, allowing the system to simultaneously probe three distinct regions of the sample.

The light reflects back from both the micromirrors and each interface within the layered sample. These reflected beams are recombined at the beam splitter and directed toward three detectors located at the bottom. The three micromirrors in the reference arm allow for independent adjustment of the reference path length for each channel, ensuring optimal interference conditions and high sensitivity for each individual beam, even if the sample regions differ in thickness or optical properties. The presence of three detectors in this configuration enables the collection of interference signals from each channel independently without crosstalk. This prevents signal overlap and allows for simultaneous acquisition of structural information from all three sample regions. The system achieves a high degree of parallelism by assigning each beam-micromirror-detector channel to a specific region or depth. This configuration is especially advantageous for applications requiring fast, multi-point imaging.

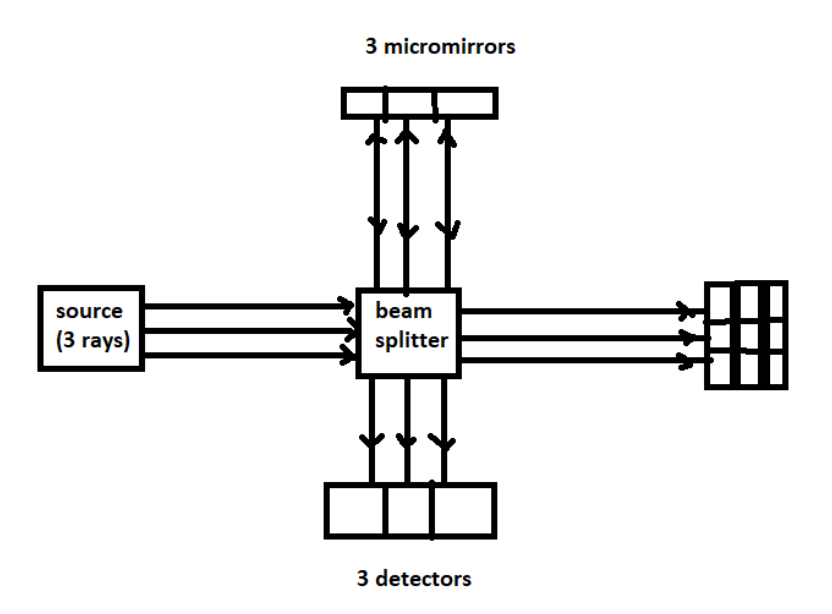


Figure 3.7: 3-Beam Michelson Interferometer Configuration

3.2.5 Four-Beam Configuration with Three Micromirrors

This Michelson interferometer setup, is engineered for advanced multi-path interference analysis, which is especially effective in OCT systems requiring high-resolution depth profiling and parallel imaging. In this configuration, a light source emits four rays simultaneously, which are directed into a central beam splitter. The beam splitter divides these rays into two paths: one set of four rays is directed upward toward four independently controlled micromirrors (forming the reference arms), while the other set is directed rightward toward a sample composed of three layers, each with distinct refractive indices. In this configuration, the micromirrors are not tilted to any angle. They are positioned flat at 0°, providing a stable reference path for interference. The light reflects back from both the micromirrors and each interface within the layered sample. These reflected beams are recombined at the beam splitter and directed toward four detectors located at the bottom.

The four incident beams enable true parallel probing, allowing simultaneous acquisition of data from multiple regions or depths. The system achieves a high degree of parallelism by assigning each beam-micromirror-detector channel to a specific region or depth. This enables multiple depth profiles or sample regions to be imaged at once without mechanical scanning

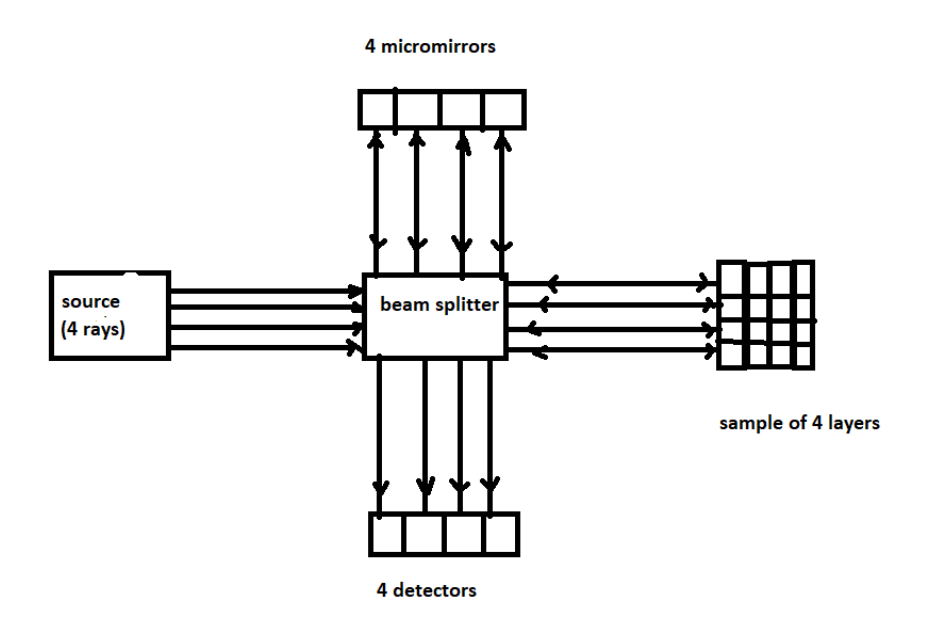


Figure 3.8: 4-beam Michelson Interferometer Configuration

In conclusion, all these setups utilize multiple beams, micromirrors, and detectors to significantly enhance the OCT systems' ability to resolve and analyze the internal structure of layered samples with varying refractive indices, providing superior depth profiling, improved parallelism, and high-speed structural imaging in real-time OCT applications.

3.2 <u>Simulation and Analysis Using COMSOL Multiphysics</u>

This chapter presents the design and simulation of a Michelson interferometer adapted to model the depth-resolving principle of OCT. The goal was to extract internal structural information from a multilayer sample by simulating interference patterns generated via low-coherence interferometry.

3.3.1 <u>Interferometer Setup in COMSOL</u>

The simulation was performed in 3D using COMSOL Multiphysics *Ray Optics Module*, *Geometrical Optics (gop)* interface. Light propagation was modeled using *Ray tracing*, which allowed precise control over the optical path difference (OPD) between the reference and sample arms. This setup enabled the observation of interference patterns at the detector screen. For detailed steps on how the Michelson interferometer was set up in COMSOL, refer to Annex.

The parameters used for the simulation are listed in the table below:

Name	Expression	Value	Description
lam	800[nm]	8E-7 m	Wavelength of He-Ne laser
delta_d	60*10*lam	4.8E-4 m	Optical path length difference
th	0.12[in]	0.003048 m	Thickness of mirrors
dia	0.5[in]	0.0127 m	Diameter of mirrors
d1	2.335[in]	0.059309 m	Distance between sample and the center of the beam splitter
d2	d1-delta_d	0.058829 m	Distance between mirrors and the center of the beam splitter
dE	12[in]	0.3048 m	Distance between the beam splitter and the screen
n_int	3.9641	3.9641	Refractive index of the beam-splitter interface
n_coat	1.2354	1.2354	Refractive index of the anti-reflective coating

Figure 3.9: Parameters for the configuration of the Michelson interferometer in COMSOL

The beam splitter was modeled with SCHOTT N-BK7 optical glass, and the mirrors, representing the micromirrors in the setup, were modeled using aluminum to provide high reflectivity. A ray detector surface from the *Geometrical Optics* (*gop*) interface was used as the detector to capture and analyze the resulting interference pattern. The light source in this configuration is a monochromatic source with a wavelength of 800 nm. In COMSOL, this was implemented using the *Release from Grid* feature within the *Geometrical Optics* (*gop*) interface, which allows for the definition of laser-like sources by specifying parameters such as wavelength, divergence, and beam origin.

The value of *delta_d* (optical path length difference) was adjusted multiple times during the simulation to change the position of the mirrors in the reference arm and observe its effect on the interference fringes.

3.3.2 <u>Configuration of a single-beam Michelson interferometer with 1</u> micromirror

The interferometer was configured with a beam splitter at the junction of two orthogonal arms: a reference arm and a sample arm. While OCT systems typically employ low-coherence or broadband sources, a monochromatic light source with a wavelength of 800 nm was used in this simulation for simplification.

In the sample arm, a test object with four layers of different refractive indices (n1=1.3, n2=1, n3=1.4, n4=1) was created to simulate a biological tissue sample. In the reference arm, a planar mirror was positioned at a distance from the beam splitter. This distance was not physically adjusted using any mechanical device, but rather, it was controlled automatically through the simulation by varying a parameter representing the optical path difference (delta_d).

The reference mirror distance (d2) as seen in table 3.1 was defined as:

$$d2 = d1 - delta_d$$

Where:

d1 is the distance from the sample to the beam splitter

delta_d is the optical path difference between the two arms, defined as a multiple of the wavelength

By changing the value of *delta_d*, the position of the reference mirror was effectively altered, allowing us to simulate different OPDs (Optical Path Differences) without moving physical components.

a) Methodology for Depth Profile Extraction

In OCT, interference fringes are produced only when the OPD (Optical Path Difference) between the reference and sample beams is within the coherence length of the light source. In the simulation, this OPD was varied by updating the *delta_d* parameter, which automatically changed the mirror position *d2* in the model.

At each value of *delta_d*, a ray tracing simulation was run, and the intensity of the resulting interference pattern was recorded at a detector screen placed after the beam splitter. The intensity value was specifically extracted from the central fringe, where the path lengths are most closely aligned, and was analyzed to detect constructive and destructive interference.

By recording the intensity at the central fringe across successive simulations with varying OPD, we obtained an intensity profile that follows the characteristic sinusoidal pattern of interferometric signals. This profile was then used to extract depth information from the sample.

b) Signal Processing and Layer Detection

To simulate OCT axial scanning (A-scan), we recorded the intensity values of the central fringe as the parameter $delta_d$ was varied. This parameter controlled the Optical Path Difference (OPD) between the reference and sample arms. The resulting intensity data was then plotted against $delta_d$ to visualize the change in interference signal with OPD. Upon plotting, we observed that the envelope of the signal followed a cosine-like modulation, superimposed with high-frequency oscillations.

This envelope contained critical information about the internal structure of the sample. To extract a clearer depth profile, we manually removed the cosine carrier that modulated the raw signal. Specifically, we divided the recorded intensity by the function:

The constant 1150 was determined empirically by testing different values and selecting the one that yielded the clearest and most accurate depth profile. It corresponds to the apparent modulation period of the high-frequency carrier present in the raw interferometric signal. This operation effectively flattened the cosine modulation, leaving behind a clean envelope with four distinct peaks, each corresponding to a reflection from a refractive index boundary within the layered sample.

All data processing, including the plotting of intensity against delta_d, division by the cosine function, and extraction of the envelope and depth profile, was carried out using Microsoft Excel.

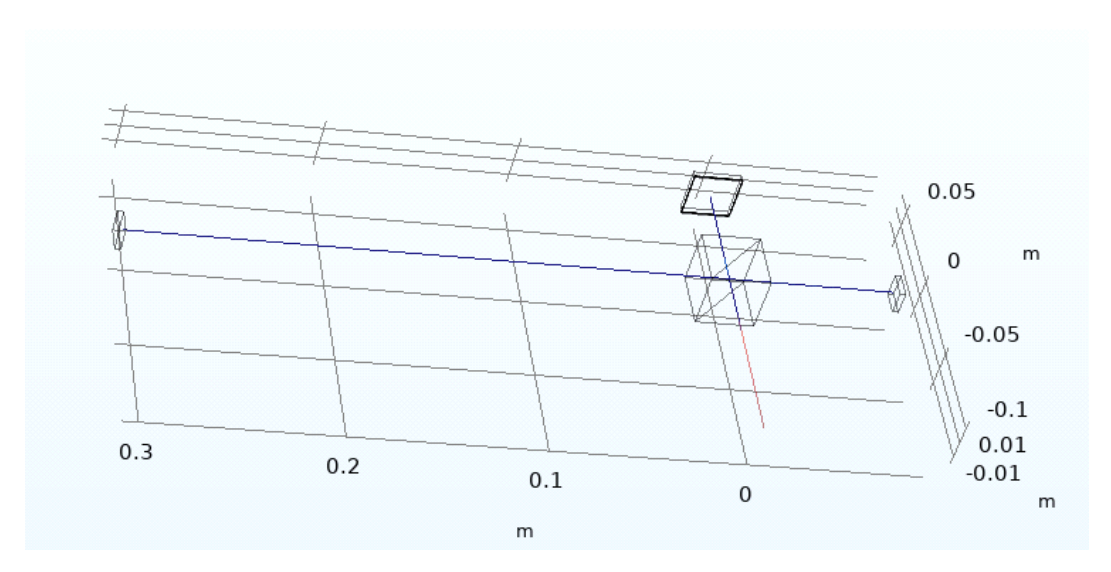


Figure 3.10: Single-beam Michelson interferometer

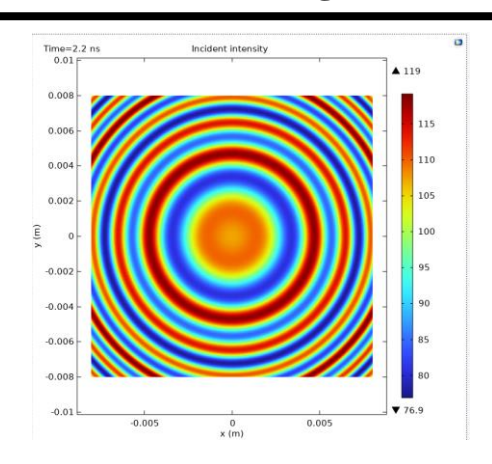


Figure 3.11: Interference pattern at delta_d=600 x lam

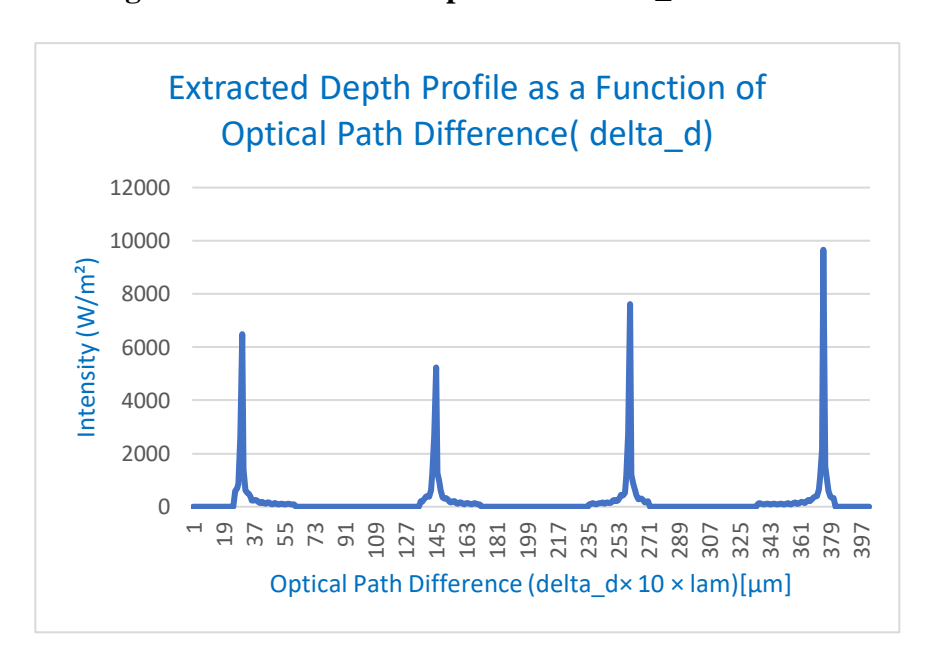


Figure 3.12: Extracted depth profile showing intensity as a function of optical path difference $(delta_d)$

3.3.3 <u>Configuration of multiple-beam Michelson interferometer with a micromirror array.</u>

In the extended simulation configuration, multiple light beams were directed to distinct regions of the sample using individually controlled micromirrors. To ensure high interference contrast and to prevent signal overlap between channels, only one beam was activated at a time while the others were disabled. Each active ray interacted with its designated region of the multilayer sample, encountering interfaces between materials of different refractive indices. The returning signal was directed to a dedicated detector associated with that beam path. For each beam-detector pair, the depth-resolving OCT procedure was performed independently to ensure spatially localized information retrieval.

The signal processing steps applied to each beam followed a standardized four-step OCT methodology:

- Varying the optical path difference (OPD) between the sample and reference arms;
- Recording the intensity of the central interference fringe at the detector;
- Plotting the fringe intensity as a function of OPD; and
- Extracting the envelope of the resulting signal to isolate structural information.

From the extracted envelope, distinct peaks were identified, each corresponding to a reflection from an internal interface within the sample. These peaks indicated variations in refractive index. By applying this process sequentially across all beam paths, it was possible to reconstruct the depth profiles of multiple spatial regions in the sample with high specificity and without mutual interference.

A critical requirement in this architecture is the use of a separate detector for each beam. In a multi-beam interferometric system, sending all returning beams to a single detector would produce overlapping interference signals. This signal superposition results in signal interference and loss of spatial discrimination, making it difficult or impossible to isolate reflections from individual sample regions. By assigning one detector to each beam, interference signals remain independent and accurately reflect the optical path differences specific to each micromirror-

sample pair. This isolation is essential for preserving the integrity of OCT measurements and is consistent with time-division multiplexing strategies employed in advanced OCT systems.

In the following section, various simulation configurations involving 2, 3, and 4 micromirrors, each paired with corresponding laser beams and detectors are presented to demonstrate the flexibility and performance of the proposed architecture.

a) Configuration of a dual-beam Michelson interferometer with beams

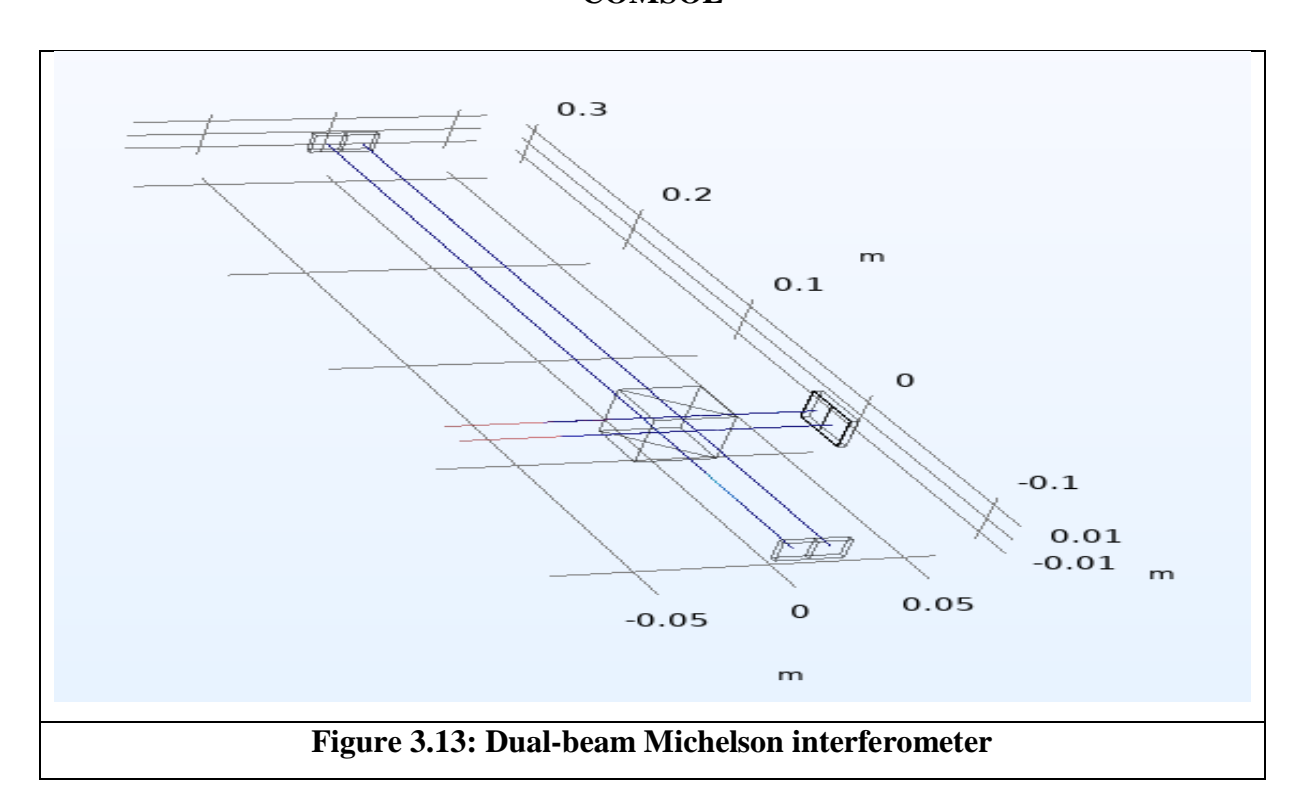
In this simulation, the reference arm contained two mirrors representing independently controlled micromirrors, while the sample arm consisted of a multilayer structure with three layers of differing refractive indices. Two detectors were used, each dedicated to capturing the interference signal from one beam path. The simulation and data extraction process followed the methodology described in Section 3.2.2. To avoid signal overlap and ensure accurate interference analysis, only one beam was activated at a time.

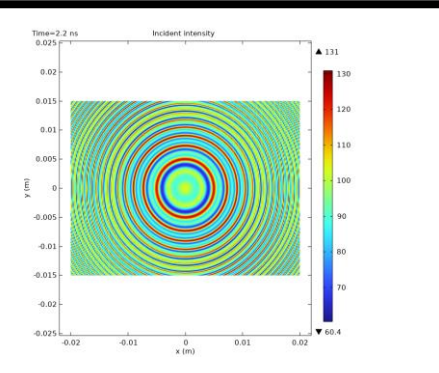
The optical path difference (OPD) was varied by adjusting the parameter delta_d which automatically altered the position of the reference mirror. For each active beam, the intensity of the central fringe in the resulting interference pattern was recorded at every *delta_d* value. The corresponding detector collected this intensity data, which was then used to extract structural information about the specific sample region probed by that beam. This enabled depth-resolved imaging of the layered structure with spatial separation and minimal cross-interference.

Chapter 3: Design, Implementation and Simulation of a Michelson Interferometer based on Digital Micromirrors

Michelson	Ray being	Interference	Refractive	Depth profile
interferometer	simulated	pattern when	indices of area	
configuration		OPD=600 x lam	being probed in	
			the sample	
Configuration of	Ray 1	Figure 3.14	n1=1.3	Figure 3.16
the Michelson			n2=1.5	
interferometer			n3=1.45	
with 2 laser	Ray 2	Figure 3.15	n1=1.5	Figure 3.17
beams, 2			n2=1.3	
micromirrors,			n3=1.45	
and a sample of				
3 layers				

 $\begin{tabular}{ll} \textbf{Table 3.1: Parameters for the configuration of a dual-beam Michelson interferometer in } \\ \textbf{COMSOL} \\ \end{tabular}$





0.025 0.035 0.001 0.001 0.002 0.001 0.001 0.002 0.001

Figure 3.14: Interference pattern of Ray 1 at *delta_d=600* x lam

Figure 3.15: Interference pattern of Ray 2 at *delta_d=600* x lam

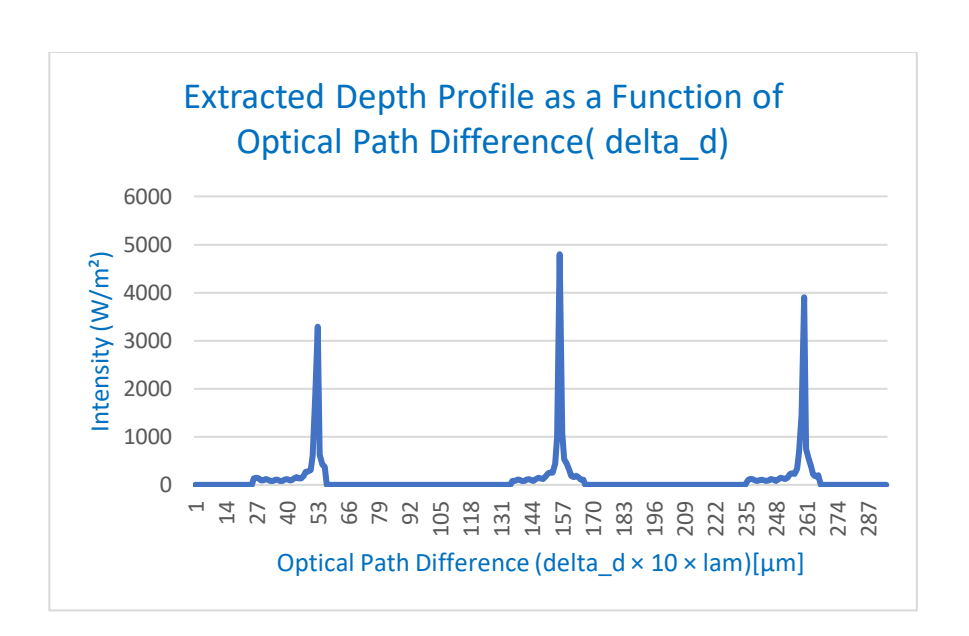


Figure 3.16: Extracted depth profile showing intensity as a function of optical path difference (delta_d) for Ray 1

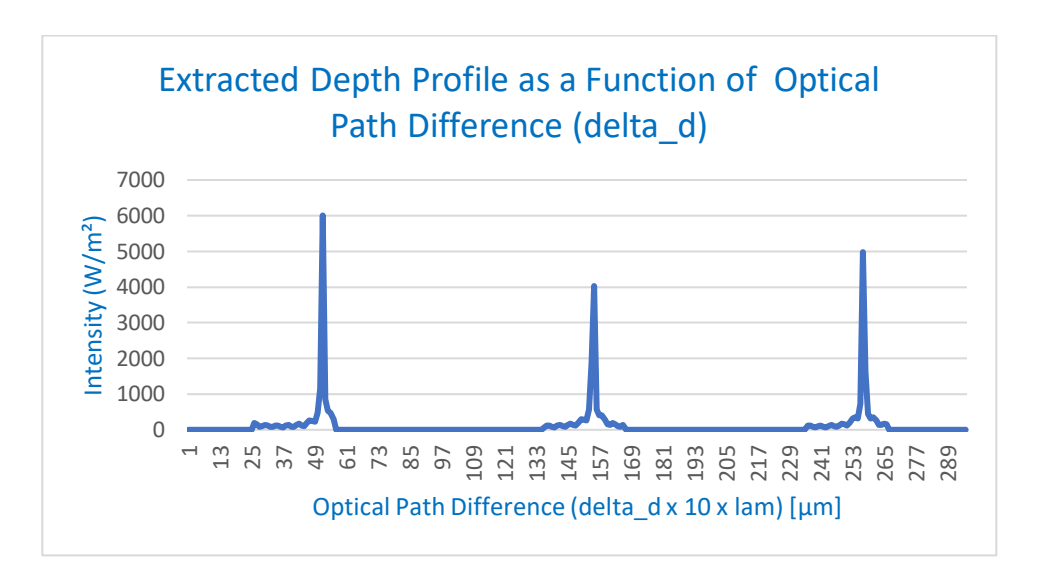


Figure 3.17: Extracted depth profile showing intensity as a function of optical path difference (delta_d) for Ray 2

b) Configuration of a dual-beam the Michelson interferometer

In this simulation, the reference arm contained two mirrors representing independently controlled micromirrors, while the sample arm consisted of a multilayer structure with four layers of differing refractive indices. Two detectors were used, each dedicated to capturing the interference signal from one beam path. One beam was activated at a time. To vary the OPD, the parameter *delta_d* was incrementally adjusted. At each delta_d value, the intensity of the central fringe formed in the resulting interference pattern was recorded. This intensity profile was then processed to extract structural information about the sample, allowing identification of internal interfaces based on variations in refractive index.

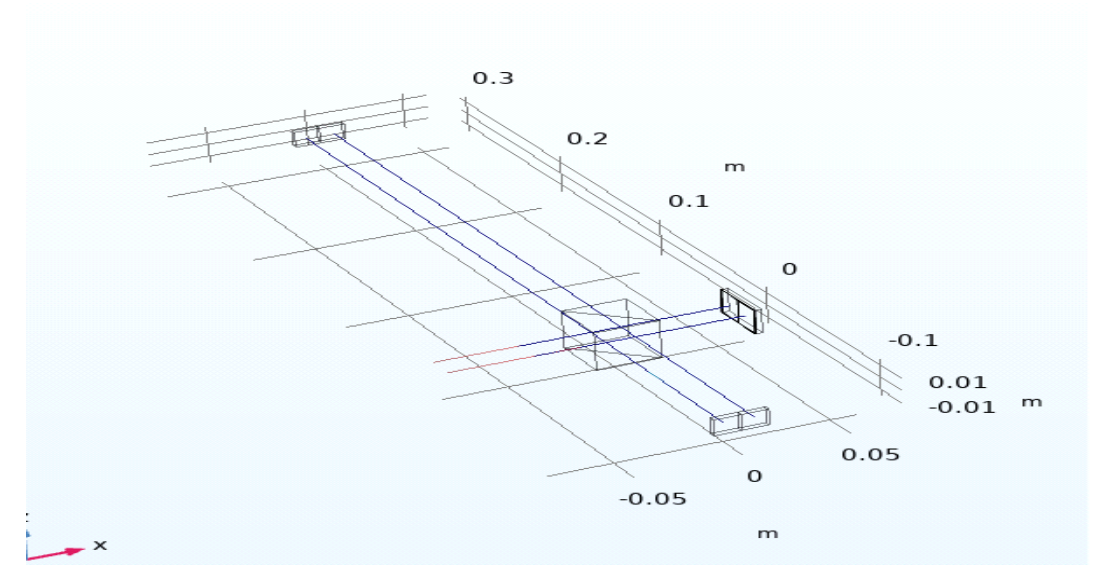


Figure 3.18: Dual-beam Michelson interferometer

Michelson	Ray being	Interference	Refractive	Depth profile
interferometer	simulated	pattern when	indices of area	
configuration		OPD=600 x lam	being probed in	
			the sample	
Configuration of	Ray 1	Figure 3.19	n1=1.3	Figure 3.21
the Michelson			n2=1.5	
interferometer			n3=1.45	
with 2 laser			n4=1.38	
beams, 2	Ray 2	Figure 3.20	n1=1.5	Figure 3.22
micromirrors,			n2=1.3	
and a sample of			n3=1.45	
4 layers			n4=1.41	

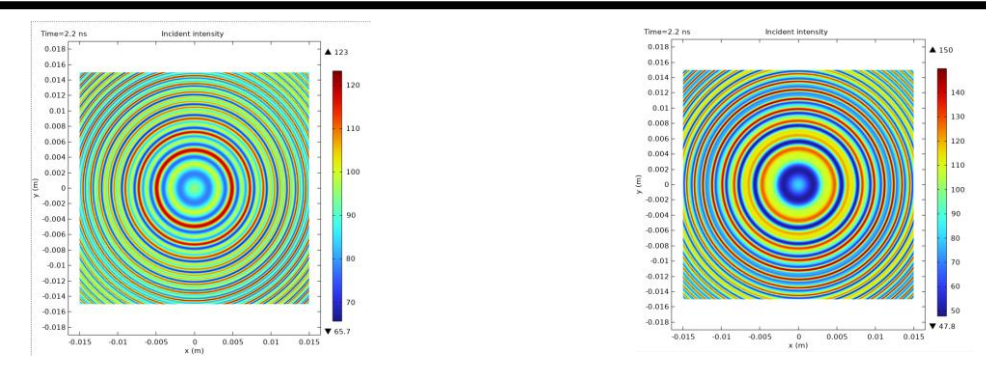


Figure 3.19: Interference pattern of Ray 1 Figure 3.20: Interference pattern of Ray 2 at delta_d=600 x lam at delta_d=600 x lam

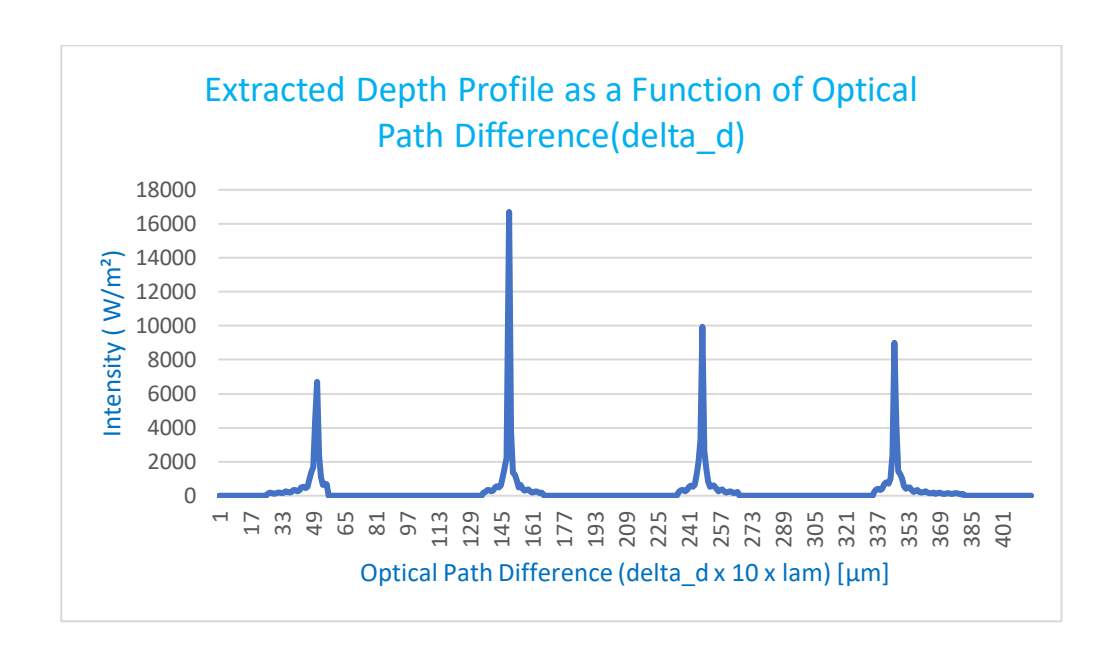


Figure 3.21: Extracted depth profile showing intensity as a function of optical path difference (delta_d) for Ray 1

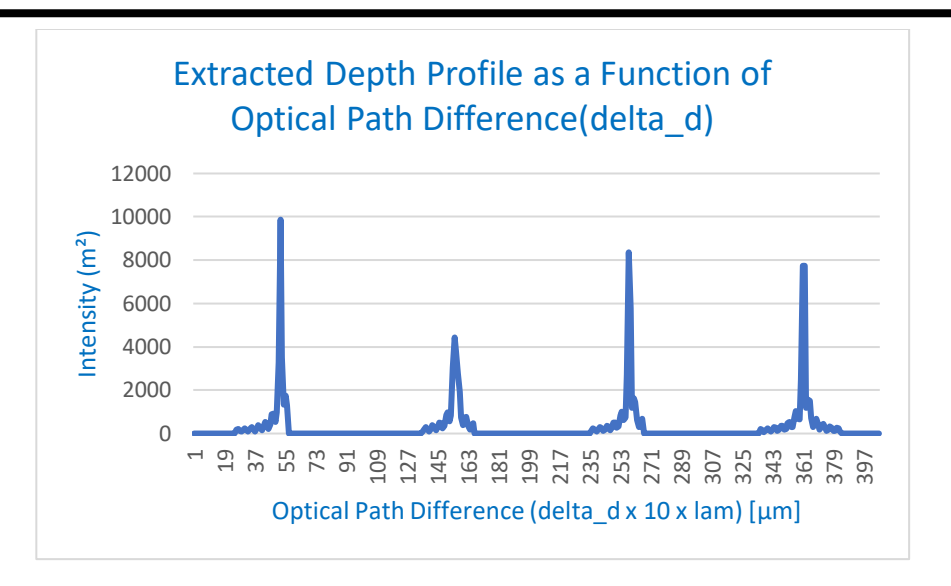


Figure 3.22: Extracted depth profile showing intensity as a function of optical path difference (delta_d) for Ray 2

c) <u>Configuration of 3-beam Michelson interferometer</u>

In this simulation, the reference arm contained three mirrors representing independently controlled micromirrors, while the sample arm consisted of a multilayer structure with three layers of differing refractive indices. Three detectors were used, each dedicated to capturing the interference signal from one beam path. To avoid signal overlap and ensure accurate interference analysis, only one beam was activated at a time.

The OPD was varied by incrementally adjusting the parameter *delta_d* which controlled the position of the reference mirror. At each *delta_d* value, the intensity of the central fringe in the resulting interference pattern was recorded by the corresponding detector. This intensity profile was then processed to extract structural information about the specific region of the sample probed by that beam, enabling the identification of internal interfaces based on refractive index variations.

Chapter 3: Design, Implementation and Simulation of a Michelson Interferometer based on Digital Micromirrors

Michelson	Ray being	Interference	Refractive	Depth profile
interferometer	simulated	pattern when	indices of area	
configuration		OPD=600 x lam	being probed in	
			the sample	
Configuration of	Ray 1	Figure 3.24	n1=1	Figure 3.27
the Michelson			n2=1.35	
interferometer			n3=1.41	
with 3 laser	Ray 2	Figure 3.25	n1=1.3	Figure 3.28
beams, 3			n2=1.38	
micromirrors,			n3=1.39	
and a sample of	Ray 3	Figure 3.26	n1=1.3	Figure 3.29
3 layers			n2=1.36	
			n3=1.4	

Table 3.3: Parameters for a 3-beam Michelson interferometer configuration in COMSOL

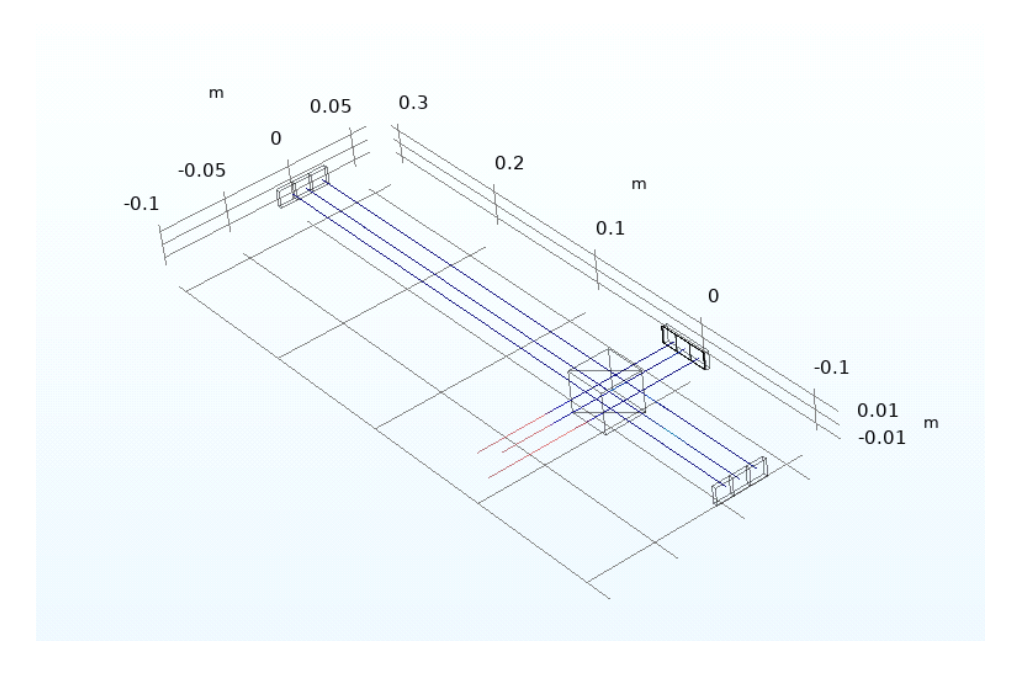


Figure 3.23: 3-beam Michelson interferometer

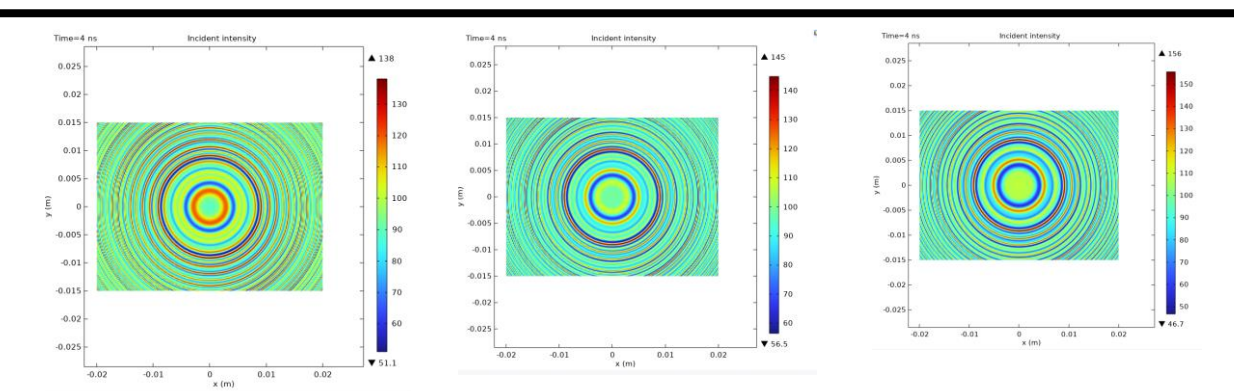


Figure 3.24: Interference pattern of Ray 1 at delta_d=600 x lam

Figure 3.25: Interference pattern of Ray 2 at delta_d=600 x lam

Figure 3.26: Interference pattern of Ray 13at delta_d=600 x lam

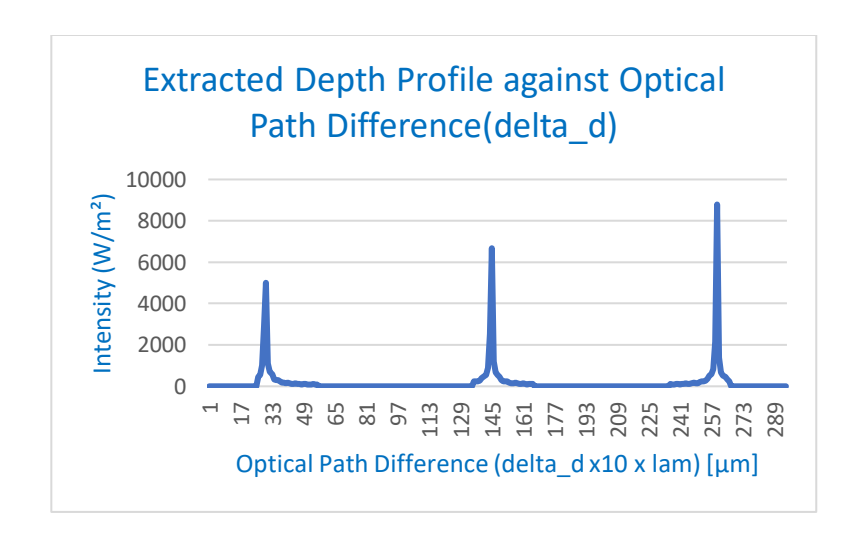


Figure 3.27: Extracted depth profile showing intensity as a function of optical path difference (delta_d) for Ray 1

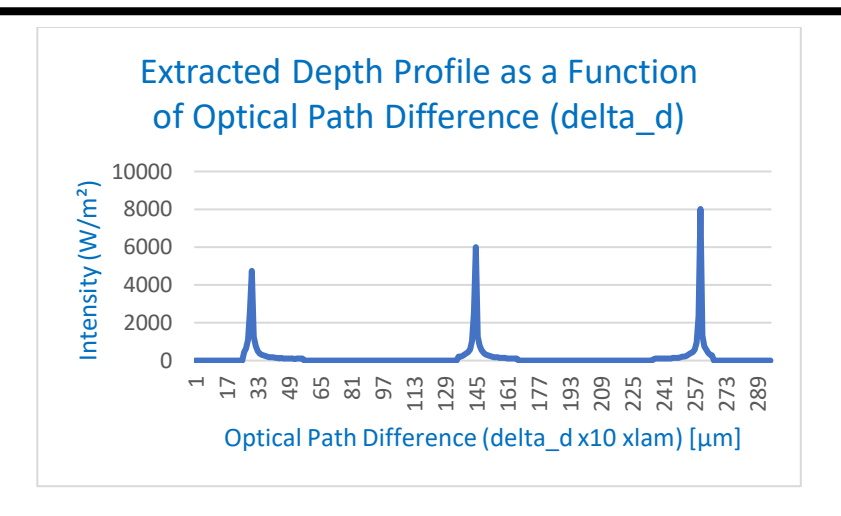


Figure 3.28: Extracted depth profile showing intensity as a function of optical path difference (delta_d) for Ray 2

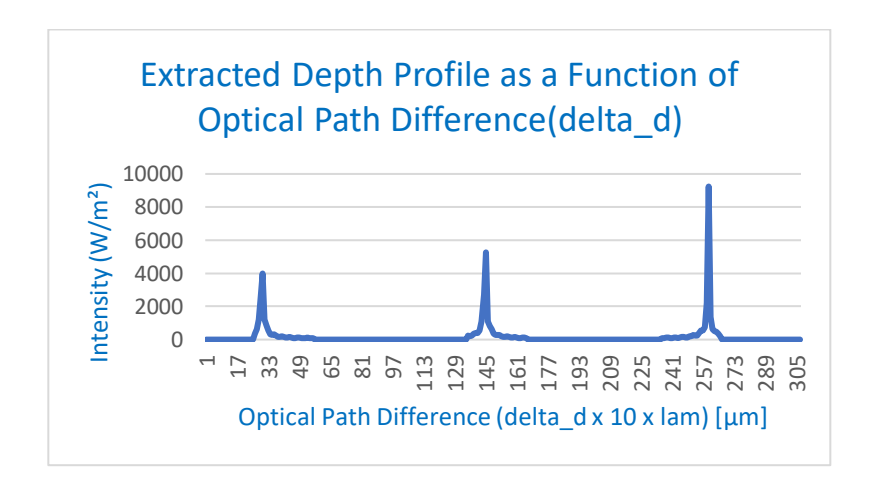


Figure 3.29: Extracted depth profile showing intensity as a function of optical path difference (delta_d) for Ray 3

d) <u>Configuration of the Michelson interferometer with 4 laser beams, 4 micromirrors,</u> and a sample of 4 layer

In this simulation setup, the reference arm was equipped with four independently actuated mirrors, each representing a micromirror. The sample arm included a multilayer structure composed of three distinct layers with varying refractive indices. Four detectors were positioned such that each one received light from a unique beam path, ensuring isolated signal detection for each channel.

To maintain signal clarity and prevent interference between beam paths, the simulation was conducted by activating one beam at a time. The optical path difference (OPD) was systematically varied by modifying the parameter $delta_d$, which dynamically repositioned the corresponding reference mirror. For each $delta_d$ value, the intensity of the central interference fringe was recorded by the associated detector. This collected intensity data was then analyzed to reveal the internal structure of the probed region in the sample, allowing precise identification of boundaries between layers based on their refractive index contrast.

Michelson	Ray being	Interference	Refractive	Depth profile
interferometer	simulated	pattern when	indices of area	
configuration		OPD=600 x lam	being probed in	
			the sample	
Configuration of	Ray 1	Figure 3.31	n1=1.3	Figure 3.35
the Michelson			n2=1.38	
interferometer			n3=1.4	
with 4 laser	Ray 2	Figure 3.32	n1=1.3	Figure 3.36
beams, 4			n2=1.36	
micromirrors,			n3=1.4	
and a sample of	Ray 3	Figure 3.33	n1=1.3	Figure 3.37
3 layers			n2=1.38	
			n3=1.3	
	Ray 4	Figure 3.34	n1=1	Figure 3.38
			n2=1.35	
			n3=1.41	

Table 3.4: Parameters for a 4-beam Michelson interferometer configuration in COMSOL

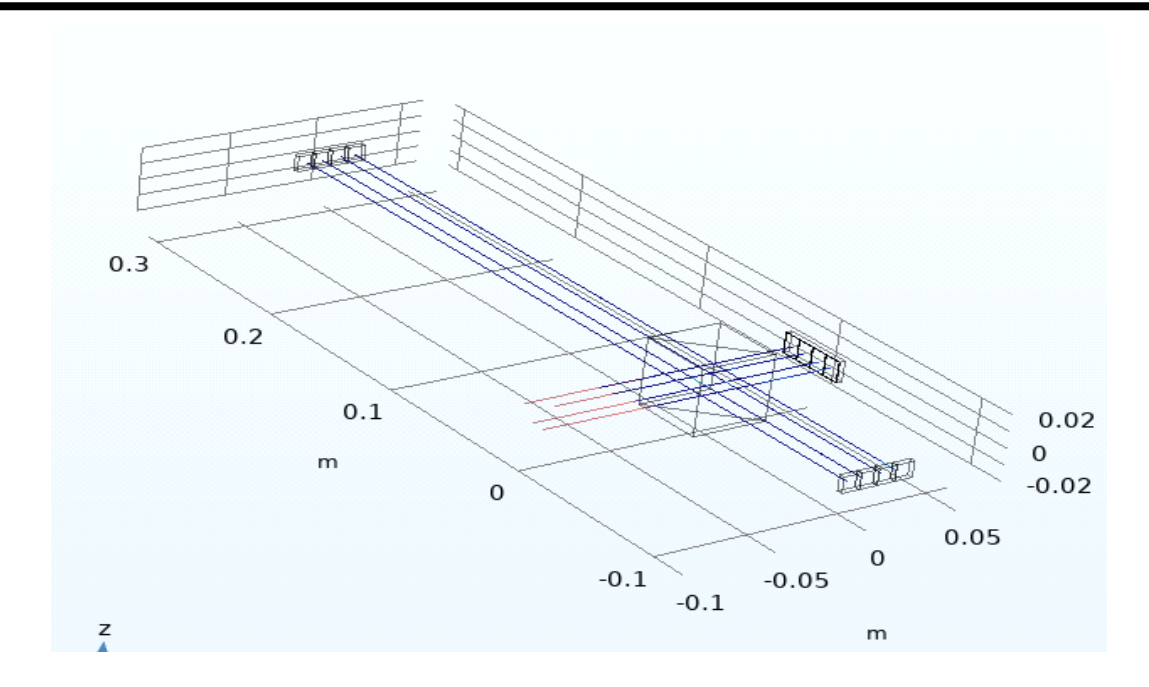
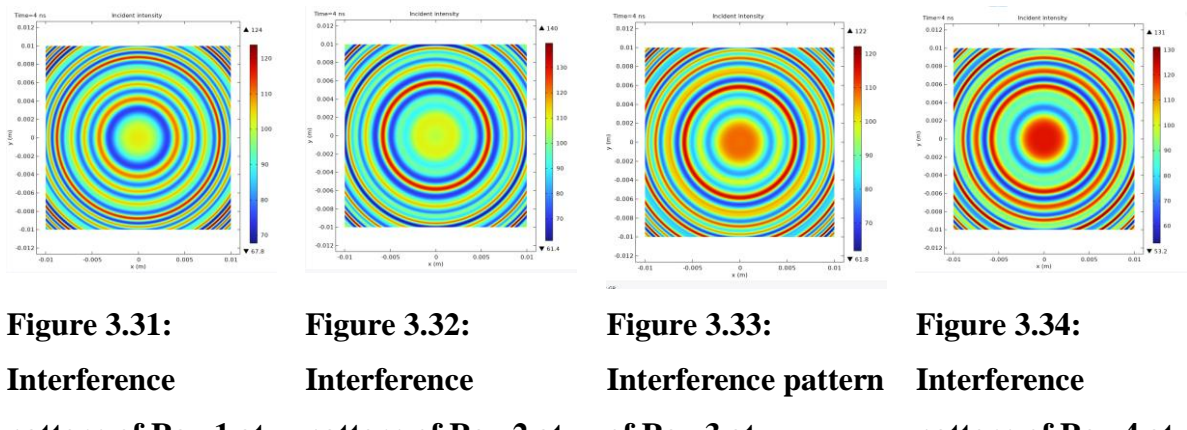


Figure 3.30: 4-beam Michelson interferometer configuration



pattern of Ray 1 at $delta_d=600 \text{ x lam}$

pattern of Ray 2 at delta_d=600 x lam

of Ray 3 at $delta_d=600 \text{ x lam}$ pattern of Ray 4 at $delta_d=600 \text{ x lam}$

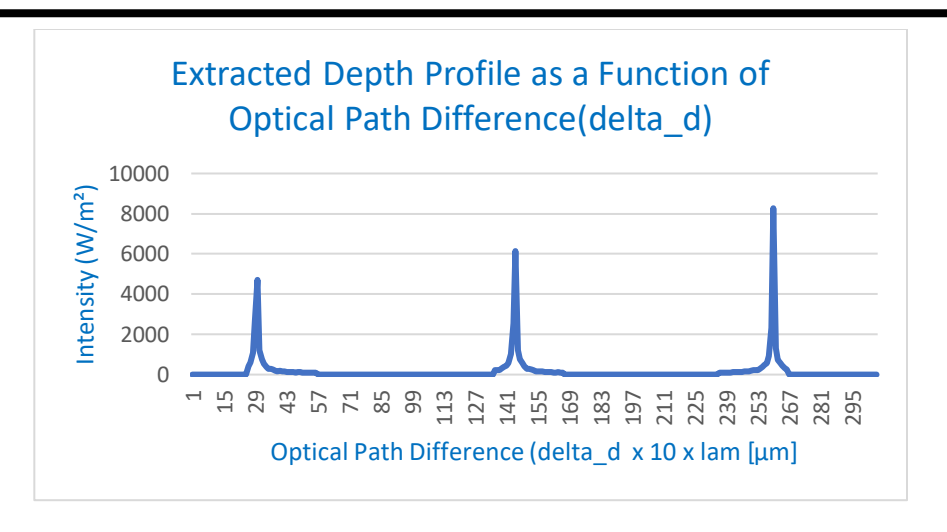


Figure 3.35: Extracted depth profile showing intensity as a function of optical path difference (delta_d) for Ray 1

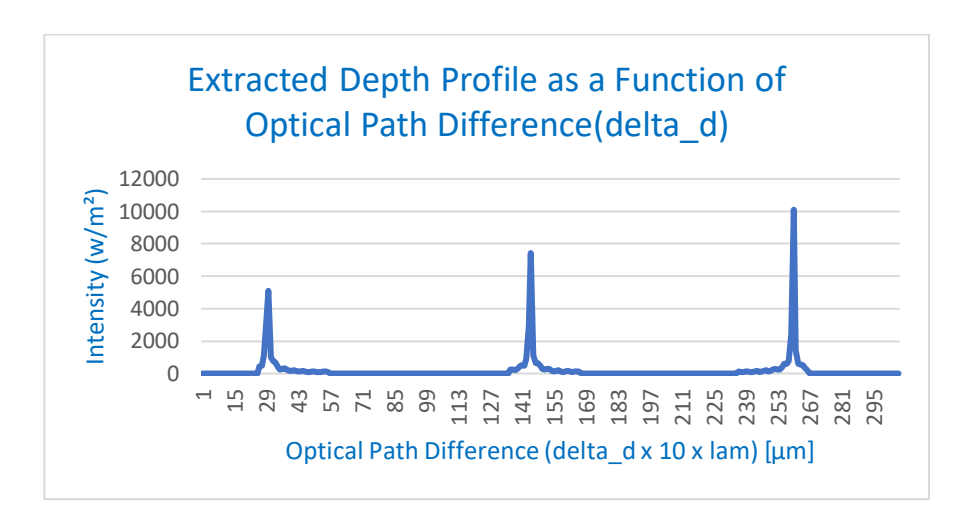


Figure 3.36: Extracted depth profile showing intensity as a function of optical path difference (delta_d) for Ray 2

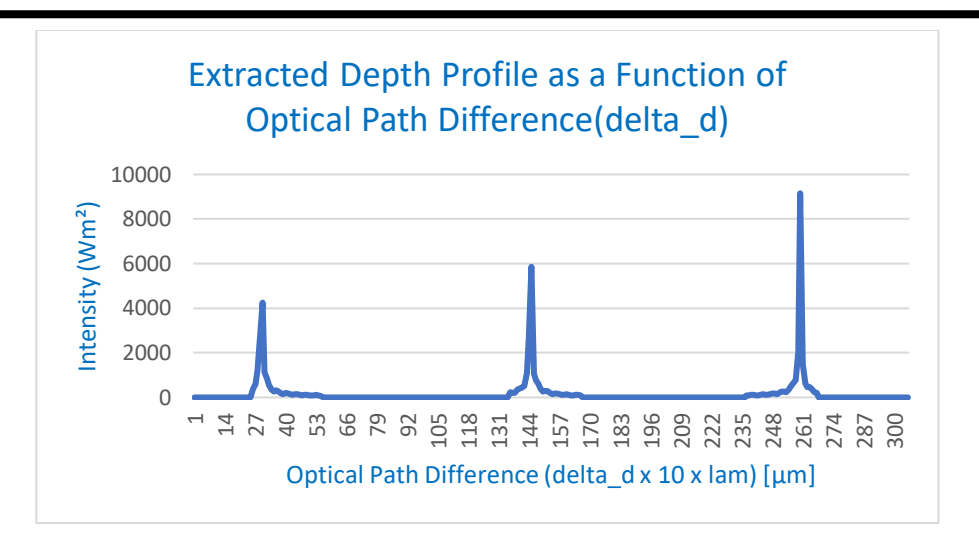


Figure 3.37: Extracted depth profile showing intensity as a function of optical path difference (delta_d) for Ray 3

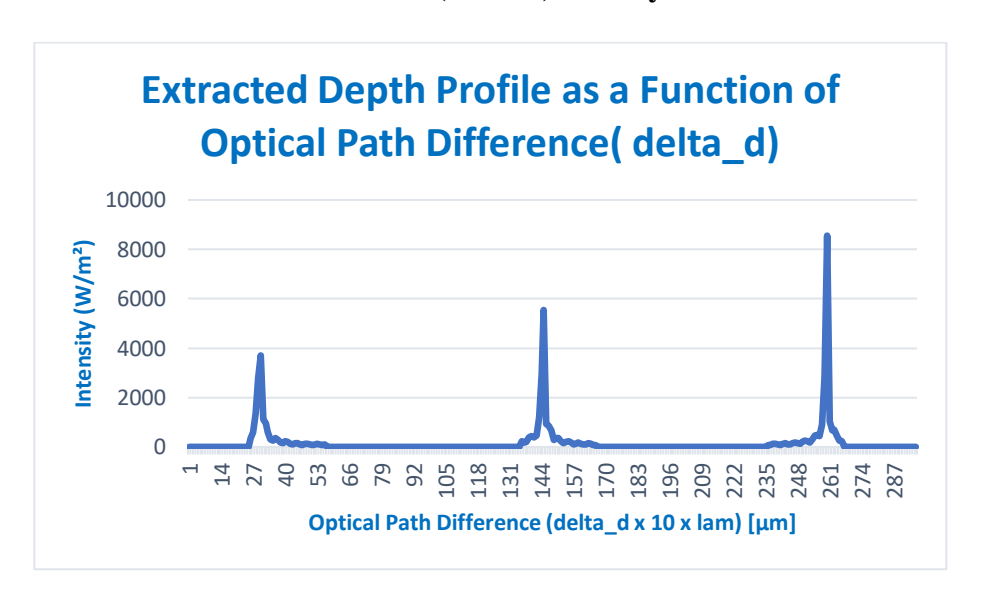


Figure 3.38: Extracted depth profile showing intensity as a function of optical path difference (delta_d) for Ray 4

3.3 Discussion of results

In this research project, we explored the design, implementation, and simulation of a Michelson interferometer architecture enhanced with digital micromirrors. This innovative approach could (after validation) enable dynamic control of the optical path in the reference arm, offering key advantages for applications such as Optical Coherence Tomography (OCT).

We began by designing several configurations of the Michelson interferometer, gradually evolving from a single-beam system to a four-beam system. Each configuration uses micromirrors to replace static reference mirrors, enabling precise control and parallel data acquisition. These configurations demonstrated how replacing traditional optical components with programmable micromirrors enhances system flexibility and imaging performance.

In this work, our study and design were conducted at a macroscopic scale, without considering the microscopic dimensions of the various components of the Michelson interferometer. Based on the results obtained, it will subsequently be easier to address smaller scales.

Simulations carried out in COMSOL Multiphysics confirmed the feasibility of these designs. Using a 3D ray optics framework, we replicated the behavior of the interferometric system while probing multilayer samples. By adjusting the optical path difference through simulation parameters rather than mechanical displacement, we accurately modeled the principle of low-coherence interferometry at the core of OCT. The simulations enabled the capture of interference patterns and the extraction of depth profiles by processing the recorded intensity data.

Through these simulations, we demonstrated that micromirror-based configurations allow simultaneous scanning of different sample regions, thus minimizing acquisition time and enabling real-time imaging. The use of distinct detectors for each beam preserved signal integrity.

We highlighted the transformative potential of digital micromirrors in optical interferometry. Not only do they offer an adaptable and parallel approach to layered structure imaging, but they also enable more compact, efficient, and potentially more cost-effective OCT systems.

It is important to note that the results obtained directly support our main objective: parallelization of OCT using micromirrors in the reference arm of the Michelson interferometer. By replacing static mirrors with programmable micromirrors and demonstrating the independent functioning of multiple beam—micromirror—detector paths, we validated the ability to acquire multiple Ascans in parallel in real time. This architecture not only meets the functional requirements of OCT parallelization but also lays the groundwork for advanced, high-speed, and miniaturized OCT systems capable of dynamic imaging in biomedical and industrial applications.

3.4 General conclusion

We did not accomplish everything we had outlined in our specifications; however, we were able to confirm that the parallelization is possible with the integration of micromirrors into OCT systems. We developed a version of the Michelson interferometer that is actually a set of micro-interferometers, which can manipulate light rays from an optical source in parallel. The results we obtained are very conclusive and encouraging; however, further validation of this work is still needed.

This work can and should be pursued further by future Master 2 students to continue the development of the architectures proposed in Chapter 3. They may also revisit our version of the Michelson interferometer and carry out the necessary studies with the aim of miniaturizing this design to the microscopic scale.

At the end of this research, we were able to demonstrate that digital micromirrors can effectively be integrated into the Michelson interferometer architecture to enable parallel, depth-resolved imaging of multilayer samples. Through the design and simulation of single-beam and multi-beam configurations, we showed that precise control of the optical path in each channel is possible using independently actuated micromirrors. This confirms the feasibility of achieving simultaneous A-scan acquisitions across different regions of a sample, an essential step towards real-time, high-resolution Optical Coherence Tomography (OCT).

Bibliography

Bibliography

- [1] M. Born and E. Wolf, Principles of Optics: Electromagnetic Theory of Propagation, Interference and Diffraction of Light, 7th ed. Cambridge, UK: Cambridge University Press, 1999.
- [2] [Z. Yaqoob, J. Wu, and C. Yang, "Spectral domain optical coherence tomography: A review of instrumental and signal processing techniques," BioTechniques, vol. 39, no. 6, pp. S6–S13, Dec. 2005.
- [3] B. Povazay et al., "Submicrometer axial resolution optical coherence tomography," Opt. Lett., vol. 27, no. 20, pp. 1800–1802, Oct. 2002.
- [4] W. Liang, M. T. Tsai, Y. Wang, and X. Li, "Dynamic focus control in high-speed optical coherence tomography based on a microelectromechanical mirror," *Opt. Lett.*, vol. 30, no. 18, pp. 2309–2311, Sep. 2005.
- [5] F. Karaoui, N. Benbildia, and H. Bougherira, "A COMSOL novel micromirror matrix model for digital image display," Engineering Research Express, vol. 6, no. 1, p. 015317, Mar. 2024.
- [6] M. C. Wu, O. Solgaard, and J. E. Ford, "Optical MEMS for light wave communication," J. Lightwave Technol., vol. 24, no. 12, pp. 4433–4454, Dec. 2006.
- [7] D. Hah et al., "Design and fabrication of a novel microelectromechanical systems (MEMS) micromirror for optical coherence tomography," IEEE J. Sel. Top. Quantum Electron., vol. 10, no. 3, pp. 505–511, May–Jun. 2004.
- [8] R. R. Iyer et al., "Phase-sensitive optical coherence tomography using a microelectromechanical mirror for optical path length modulation," Opt. Lett., vol. 31, no. 12, pp. 1802–1804, Jun. 2006.
- [9] B. Povazay et al., "Parallel optical coherence tomography: ultra-high-speed and multi-channel imaging," Opt. Lett., vol. 27, no. 20, pp. 1800–1802, Oct. 2002.
- [10] B. H. Park et al., "Real-time fiber-based multi-channel optical coherence tomography," Opt. Express, vol. 12, no. 21, pp. 5130–5137, Oct. 2004.

- [11] Y. Luo, L. J. Arauz, J. E. Castillo, J. K. Barton, and R. K. Kostuk, "Parallel optical coherence tomography system," Appl. Opt., vol. 46, no. 34, pp. 8291–8297, Dec. 2007.
- [12] COMSOL AB, "Michelson Interferometer," *COMSOL Multiphysics Application Gallery (Ray Optics Module tutorial), 2023.
- [13] A. Taflove, A. Oskooi, and S. G. Johnson, *Optics Modeling and Visualization with COMSOL Multiphysics*, Cambridge Univ. Press, 2019
- [14] D. Huang et al., "Optical coherence tomography," Science, vol. 254, no. 5035, pp. 1178–1181, Nov. 1991.
- [15] X. Liu, M. Daneshpanah, M. S. Shahriar, and J. C. Chiao, "MEMS-based Optical Coherence Tomography," in Proc. SPIE MEMS Components and Applications for Industry, vol. 5312, pp. 180–191, May 2004,
- [16] B. Braaf, Angiography and Polarimetry of the Posterior Eye with Functional Optical Coherence Tomography, Ph.D. dissertation, Vrije Universiteit Amsterdam, 2015.
- [17] F. Boulvert, Analyse de milieux fortement diffusants par polarimétrie de Mueller et méthodes optiques cohérentes. Application à l'étude du syndrome cutané d'irradiation aiguë, Ph.D. dissertation, Université de Bretagne Occidentale, Brest, France, 2006
- [18] Z. Zhao, Y. Liu, and J. Yao, "A multi-scale dynamic weight architecture for semantic segmentation of remote sensing images," Comput. Methods Appl. Mech. Eng., vol. 400, 115504, 2022.

Annex

COMSOL Simulation Setup for the Michelson Interferometer

This annex describes the detailed steps used to set up and simulate the Michelson interferometer in COMSOL Multiphysics using the Ray Optics Module. It is intended to allow replication and validation of the results presented in Chapter 3.

1. Creating a new model in COMSOL

- Open COMSOL Multiphysics and from the File menu choose New
- In the **New** window, click **Model Wizard**
- In the Model Wizard window, click 3D
- In the Select Physics tree, select Optics>Ray Optics>Geometrical Optics (gop).
- Click **Add**.
- Then click Study.
- In the Select Study tree, select Preset Studies for Selected Physics Interfaces>Ray
 Tracing
- Click Done

2. Model Builder

- In the **Model Builder** window located on the left, go to **Global Definitions** and under it click **Parameters 1** and in the **Settings** window a table will be displayed. In this table, you can define your parameters and give these parameters names and values. The parameters you can define include distance of the sample and reference arms from the beam splitter, wavelength of your light source, optical path difference and any others of your choice.
- In the Home toolbar, click Part Libraries.
- In the Part Libraries window, select Ray Optics Module>3D>Beam splitters > beam_splitter_cube in the tree
- Click Add to Geometry.

3. Geometry

- In the Model Builder window, under Component 1 (comp1)>Geometry 1 click Beam
 Splitter Cube 1 (pi1).
- In the **Settings** window for the beam splitter, locate the **Input Parameters** section
- A table will be displayed and it you define the length of the sides of your beam splitter and the x, y and z component of your incident and reflected ray direction of the beam splitter
- In the **Geometry** toolbar, click Block
- In the **Settings** window for **Block**, locate the **Size and Shape** section. In this section you enter the width, height and depth of your block.
- Locate the **Position** section. From the **Base** list, choose **Center** and then enter the x, y and z coordinates for the position of the block. This block should be placed on the side of the beam splitter cube that will be your reference arm
- In the **Geometry** toolbar, click Block to create a second block and repeat step (6). This second block should be placed on the side of the beam splitter cube that will be your sample arm

 Create a third block that will act as your detector that will capture the rays after recombination at the beam splitter. This is also where the interference patter will be formed. Place it at a distance from your beam splitter

4. Adding materials

- In the **Home** toolbar, click Add Material to open the Add Material window. This will be displayed on the right side of your screen.
- Go to the **Add Material** window and search for any material you would like to allocate to the beam splitter cube and the 2 blocks
- Click Add to Component in the window toolbar and this will display the Settings window for this material.
- In the Settings window of the material, under Geometric entity level, choose
 domain. Under Selection choose manual and this will enable add this material for
 any of the geometric components in your setup.

5. Geometric Optics (GOP)

- In the Model Builder window, under Component 1 (comp1) click Geometrical Optics (gop).
- In the **Settings** window for **Geometrical Optics**, locate the **Intensity Computation** section.
- From the **Intensity computation** list, choose **Compute intensity and power.**
- Select the **Compute phase** check box.
- In the Model Builder window, under Component 1 (comp1)>Geometrical Optics
 (gop) click Material Discontinuity 1.
- In the **Settings** window for **Material Discontinuity**, locate the **Coatings** section.
- From the **Thin dielectric films on boundary** list, choose **Anti-reflective coating**.
- Select the **Treat as single layer dielectric film** check box.
- In the λ_0 text field, insert the wave length of your source

6. Ray properties

- Under Geometrical Optics (gop) click Ray Properties 1.
- In the **Settings** window for **Ray Properties**, locate the **Ray Properties** section.
- In the λ_0 text field, enter the wave length of your light source.
- Right click on **Geometrical Optics** (gop) and this will display a list of boundaries. Select mirror from this list.
- This will display the settings window for the mirror boundary. For selection, choose manual then in the **Graphics** window on the right, select the surfaces on each of the blocks that light will be reflected. This will place a mirror on these surfaces
- In the Physics toolbar, click Boundaries and choose Material Discontinuity.
- In the **Settings** window for **Material Discontinuity**, type Beam Splitter in the **Label** text field.
- Locate the **Coatings** section. From the **Thin dielectric films on boundary** list, choose **Specify reflectance.**
- In the R text field, enter your value of reflectance.
- In the R text field, type 0.5.
- 5 Select the **Treat as single layer dielectric film** check box.
- 6 In the n text field, type n_int.
- 7 In the λ_0 text field, enter your value for the wave length.
- 8 In the θ_i text field, type 45[deg].
- Select the boundary corresponding to the beam splitter in the beam splitter cube.

7. Release from Grid

In COMSOL Multiphysics, the 'Release from Grid' feature is used to initiate ray tracing within the simulation domain. This feature defines the initial positions and directions of rays by releasing them from a specified set of grid points on a boundary or surface. It effectively serves as the source of rays in ray optics simulations.

• Right click on Geometrical Optics (gop) and choose Release from Grid.

- In the **Settings** window for **Release from Grid**, locate the **Initial Coordinates** section and enter your x, y and z coordinates. This will be the position the ray will be released from.
- Locate the **Ray Direction Vector** section choose **expression** and then specify the L_0 vector. This will be the direction your ray will travel once it is released.
- Locate the Initial Radii of Curvature section. From the Wavefront shape list, choose
 Spherical wave.
- In the r0 text field, type -1[m]. A negative value means that the wavefront is converging and
- the rays are aimed toward a focal point
- Locate the **Initial Polarization** section. From the **Initial polarization type** list, choose **Fully polarized.**
- From the **Initial polarization** list, choose **User defined**.
- Specify the **u** vector. The **u** vector is a unit vector that defines the direction of the electric field (the polarization direction) of the emitted rays at the moment of release
- Right click on **Geometrical Optics (gop)** and choose **Ray Termination.** This feature limits the propagation of rays within the simulation.
- In the **Settings** window for **Ray Termination**, locate the **Termination Criteria** section.
- From the **Spatial extents of ray propagation** list, choose **Bounding box, from geometry.** This means that rays that travel outside this bounding box will be terminated (stopped).

8. Ray Tracing

In the Model Builder window, under Study 1 click Step 1: Ray Tracing
In the Settings window for Ray Tracing, locate the Study Settings section. In the Timestep specifications, choose specify time steps.

In the **Output times** section and click on . This will display a table. In this table, enter your start, step and stop value and then click **Replace**.

In the **Home** toolbar, click **Compute**. This will compute your solution.

9. Results

- In the **Settings** window for **Cut Plane**, locate the **Data** section.
- 3 From the **Dataset** list, choose **Ray 1**.
- 4 Locate the Plane Data section. From the Plane list, choose xz-planes.
- In the **y-coordinate** text field, enter the distance of the mirror in the reference arm from the beam splitter.

10. Interference pattern

- In the **Results** toolbar, click **2D Plot Group.**
- In the **Settings** window for **2D Plot Group**, type Interference Pattern in the **Label** text field.
- Locate the **Data** section. From the **Dataset** list, choose **Cut Plane 1**.
- In the Interference Pattern toolbar, click More Plots and choose Interference Pattern.
- In the **Settings** window for **Interference Pattern**, locate the **Coordinate Range section**.
- From the Origin location specification list, choose At ray of greatest intensity.
- In the **Interference Pattern** toolbar, click Plot. This instruction will plot your interference pattern on the screen.

11. Parametric sweep

- To perform a parametric sweep, go to Study toolbar and click
 Sweep.
- In the **Settings** window, go to **Study Settings**. In the table add a parameter, int the **Parameter value list** section write **range** (**start value**, **step value**, **end value**).
- Then compute.